



Hydrothermally induced ^{34}S enrichment in pyrite as an alternative explanation of the Late-Devonian sulfur isotope excursion in South China

Hao Yan^{a,b}, Daohui Pi^{a,*}, Shao-Yong Jiang^{a,*}, Weiduo Hao^b, Huan Cui^{d,e},
Leslie J. Robbins^c, Kaarel Mänd^{b,f}, Long Li^b, Noah J. Planavsky^c,
Kurt O. Konhauser^b

^a State Key Laboratory of Geological Processes and Mineral Resources, School of Earth Resources, China University of Geosciences, Wuhan, China

^b Department of Earth & Atmospheric Sciences, University of Alberta, Edmonton, AB, Canada

^c Department of Geology & Geophysics, Yale University, New Haven, CT, USA

^d Research Group of Analytical, Environmental and Geo-Chemistry, Division of Earth System Science, Vrije Universiteit Brussel, Brussels, Belgium

^e ET-HOME (Evolution and Tracers of the Habitability of Mars and Earth) Astrobiology Research Consortium, Belgium

^f Department of Geology, University of Tartu, Tartu, Estonia

Received 6 October 2019; accepted in revised form 18 May 2020; Available online 28 May 2020

Abstract

Several Late Devonian sedimentary successions host pyrite with highly positive sulfur isotope values ($\delta^{34}\text{S}_{\text{pyrite}}$). These anomalous values have been linked to marine anoxia, low sulfate concentrations in seawater, or aerobic re-oxidation of dissolved sulfide within well-oxygenated bottom waters in a local depositional environment. Implicit to these previous models is the assumption of a biogenic genesis from microbial sulfate reduction (MSR) of these pyrites, which, in turn, can be used to understand the biogeochemical sulfur cycle and reconstruct paleoenvironmental conditions. In South China, the Late-Devonian bulk-rock sulfur isotope excursion occurs in the lower Fammenian Wuzhishan Formation of the Youjiang Basin, in both the sedimentary limestone that corresponds to the Late *triangularis* conodont zone at the Fuhe section and the sediment-hosted Xialei Mn deposit that lies between the Late *triangularis* and *crepida* conodont zones. To further constrain the significance of these ^{34}S -enriched pyrites, we carried out detailed textural and in-situ sulfur isotope examinations of pyrites in the Xialei Mn deposit. We found one type of pyrite in siliceous limestone referred to as the host rocks and three distinct pyrite types in Mn ores: Type I – pyrites with Mn-carbonate inclusion-rich cores; Type II – pyrite overgrowths surrounding an “inclusion-rich” core; and Type III – relatively inclusion-poor and mainly subhedral disseminated pyrite grains. Type I pyrites in Mn ores have negative $\delta^{34}\text{S}_{\text{pyrite}}$ values from -7.8‰ to -2.0‰ . Types II and III pyrites, and pyrites in the host rock are characterized by highly positive $\delta^{34}\text{S}_{\text{pyrite}}$ values ($+4.2\text{‰}$ to $+37.6\text{‰}$), with some values being higher than that of contemporaneous seawater sulfate. Type I pyrites with negative $\delta^{34}\text{S}$ values likely formed via MSR in a closed porewater system, driven by increased sedimentation rates during a sea level lowstand. The other pyrites with highly positive $\delta^{34}\text{S}$ values appear to have formed during secondary hydrothermal alteration, with their sulfur sourced through thermochemical sulfate reduction (TSR) of sulfate from dissolved barites in the underlying Liujiang Formation. This implies that the positive $\delta^{34}\text{S}$ values of the Late Devonian pyrites from the Wuzhishan Formation represent a later alteration event caused by post-depositional hydrothermal

* Corresponding authors.

E-mail addresses: pdaohui@163.com (D. Pi), shyjiang@cug.edu.cn (S.-Y. Jiang).

fluids, and may lack a direct biogeochemical connection to the surface sulfur cycle. These results provide an important perspective on the origin of variability in sulfur isotope records and suggest the need for careful petrographic screening and micrometer-scale analysis of sedimentary units used to reconstruct paleoenvironmental conditions.

© 2020 Elsevier Ltd. All rights reserved.

Keywords: In-situ analysis; Positive sulfur isotopic excursion; Pyrite; Mn ores; Late Devonian; South China

1. INTRODUCTION

The global biogeochemical sulfur cycle plays an important role in regulating Earth's surface redox state and climate via various microbial metabolic processes (e.g., microbial sulfate reduction – MSR, disproportionation, and sulfide oxidation) (Berner, 1989; Berner and Raiswell, 1983; Canfield, 2001a; Fike et al., 2015; Garrels and Lerman, 1981; Holland, 1973). Our understanding of the temporal evolution of the sulfur cycle is primarily based on inferences from the stable isotopic compositions of sulfur-bearing phases preserved in sedimentary strata, including sulfate (e.g., gypsum, barium) and sulfide (e.g., pyrite) minerals (Canfield and Teske, 1996; Fike et al., 2006; Fike and Grotzinger, 2008; Fike et al., 2015; Gill et al., 2007; Hurtgen et al., 2009; Jones and Fike, 2013). In particular, pyrite is a common mineral in sedimentary rocks through time, and thus serves as an ideal target for the study of the sulfur cycle over Earth's history (e.g., Cui et al., 2018; Gomes et al., 2018; Pasquier et al., 2017; Rose et al., 2019).

In marine strata, pyrite production is often attributed to microbial sulfate reduction (MSR) based on the strong ^{34}S depletion, i.e., very negative sulfur isotope values ($\delta^{34}\text{S}_{\text{pyrite}}$) found in most sedimentary pyrites – a result of the kinetic isotopic effect associated with MSR in which ^{32}S is preferentially incorporated into the pyrite product (e.g., Böttcher, 2011; Canfield, 2001a,b, 2004; Canfield and Farquhar, 2012; Ohmoto and Goldhaber, 1997; Sim et al., 2011a). Sulfur isotope fractionation between dissolved sulfate and MSR-produced sulfide ($\Delta^{34}\text{S}_{\text{sulfate-sulfide}} = \delta^{34}\text{S}_{\text{sulfate}} - \delta^{34}\text{S}_{\text{sulfide}}$; Jørgensen et al., 1992) can be higher than +40‰, and even up to +66‰, as previously observed in laboratory experiments (Canfield, 2001b; Canfield et al., 2010; Eldridge et al., 2016; Leavitt et al., 2013; Sim et al., 2011a). Larger $\Delta^{34}\text{S}_{\text{sulfate-pyrite}}$ values of up to +72‰ are related to bacterial sulfur disproportionation (Canfield, 2001a; Canfield and Teske, 1996; Fike et al., 2006; Johnston et al., 2005).

In addition to the common occurrence of negative $\delta^{34}\text{S}_{\text{pyrite}}$ values, positive $\delta^{34}\text{S}_{\text{pyrite}}$ excursions resulted from a decrease in $\Delta^{34}\text{S}_{\text{sulfate-sulfide}}$ can also be observed in the geologic record (e.g., Fike et al., 2015; Richardson et al., 2019a; Rose et al., 2019). The magnitude of $\Delta^{34}\text{S}_{\text{sulfate-sulfide}}$ during MSR is modulated by strain-specific factors (Bradley et al., 2016; Fike et al., 2015), intracellular metabolite levels (Wing and Halevy, 2014), the cell-specific sulfate reduction rates related with organic carbon loading (Gomes and Hurtgen, 2015; Leavitt et al., 2013; Sim et al., 2011b), and, most significantly, the dissolved sulfate concentration (e.g., Algeo et al., 2015; Crowe et al.,

2014; Habicht et al., 2002). Traditionally, these positive $\delta^{34}\text{S}_{\text{pyrite}}$ excursions have been explained by perturbations to the global sulfur cycle, e.g., increased pyrite burial flux associated with reducing marine conditions (Canfield, 2004; Fike and Grotzinger, 2008) or decreased ocean sulfate concentrations (Li et al., 2012; Newton et al., 2011). However, substantial spatial and stratigraphic variability in $\delta^{34}\text{S}_{\text{pyrite}}$ excursions suggests that these could also be explained simply by local changes in the depositional environment, i.e., not a global phenomenon (e.g., Fike et al., 2015). A number of recent studies have shown that the enhanced sedimentation rates could decrease the openness of the diagenetic system where pyrite commonly precipitates: in closed porewater systems (e.g., Pasquier et al., 2017; Richardson et al., 2019a). During this process, sulfate diffusion rates from the overlying water column to the porewater are too low to keep up with sulfate consumption by MSR and, as sulfate is depleted, the $\delta^{34}\text{S}$ of porewater sulfate increase, resulting in a parallel increase in $\delta^{34}\text{S}_{\text{pyrite}}$ and decrease in $\Delta^{34}\text{S}_{\text{sulfate-sulfide}}$ results (Kohn et al., 1998; McLoughlin et al., 2012; Wacey et al., 2015). Such may have occurred during sea level lowstands in local stratigraphic sections (Bryant et al., 2019; Pasquier et al., 2017; Richardson et al., 2019a; Rose et al., 2019), potentially as well as resulting in increased pyrite oxidation rates during early sediment diagenesis (Fry et al., 1988).

Nevertheless, all of the models above assume a biogeochemical origin related to MSR, but abiotic processes may also induce positive $\delta^{34}\text{S}_{\text{pyrite}}$ signals. One such process is thermochemical sulfate reduction (TSR) – the reduction of sulfate by organic matter during hydrothermal heating (>110 °C) in late- or post-burial diagenesis (e.g., Goldstein and Aizenshtat, 1994; Jiang et al., 2015, 2018; Kiyosu and Krouse, 1990; Machel, 2001; Machel et al., 1995; Worden et al., 1995). The $\Delta^{34}\text{S}_{\text{sulfate-pyrite}}$ induced by TSR has a first-order dependence on temperature (Kiyosu, 1980; Kiyosu and Krouse, 1990): at >200 °C, $\Delta^{34}\text{S}_{\text{sulfate-pyrite}}$ is ~25‰ (Ohmoto and Goldhaber, 1997) while at <200 °C, $\Delta^{34}\text{S}_{\text{sulfate-pyrite}}$ has been reported between ~40‰ (Friedman and O'Neil, 1977; Oduro et al., 2011) to ~30‰ (Ohmoto and Lasaga, 1982; Ohmoto and Goldhaber, 1997; Seal, 2006). However, sulfate concentration also controls $\Delta^{34}\text{S}_{\text{sulfate-pyrite}}$ during TSR (Meshoulam et al., 2016): low sulfate leads to quantitative sulfur isotope fractionation during TSR, resulting in ^{34}S -enriched pyrite with $\delta^{34}\text{S}$ values close to that of the sulfate source (Machel, 2001; Machel et al., 1995; Powell and Macqueen, 1984). TSR has been proposed as an alternative explanation for some Neoproterozoic “superheavy pyrites” (i.e., $\delta^{34}\text{S}_{\text{pyrite}} > \delta^{34}\text{S}_{\text{sulfate}}$; Ries et al., 2009) from the Datangpo Formation, South China (Cui et al., 2018), and

is also widely reported from hydrocarbon reservoirs, ore deposits and geological records of the early Earth (e.g., Brueckner et al., 2014; Jiang et al., 2018; Johnson et al., 2013; King et al., 2014; Qiu et al., 2018). In light of these recent developments, some positive $\delta^{34}\text{S}_{\text{pyrite}}$ records might indeed lack a direct biogeochemical connection to the surface sulfur cycle and, as such, may not be as valuable a proxy for reconstructing paleoenvironmental conditions as previously thought. A further complication is that different abiotic and microbial processes can result in remarkable pyrite zonation or heterogeneity on single-grain scales. Therefore, careful petrographic and high-resolution geochemical examinations (e.g., in-situ isotopic analysis) are needed to investigate positive $\delta^{34}\text{S}_{\text{pyrite}}$ signals in geological records.

The Late Devonian marks a critical period characterized by the Frasnian (382.7–372.2 Ma) – Famennian

(372.2–358.9 Ma) biotic crisis; from herein referred to as the F-F biotic crisis (Huang et al., 2018; Ma et al., 2016), a transformation in ocean redox conditions (Geldsetzer et al., 1987; Joachimski et al., 2001; Wang et al., 1996) and relatively low seawater sulfate concentrations (based on the gypsum evaporite record; Fig. 1a; Horita et al., 2002; Lowenstein et al., 2003). A remarkable feature of the Late Devonian chemostratigraphy is a striking positive $\delta^{34}\text{S}_{\text{pyrite}}$ excursion (Fig. 1b). This excursion, obtained from bulk-rock analyses, has been reported from multiple sections around the world even though the timing, duration, and magnitude are slightly variable between locations (Fig. 1c). These positive $\delta^{34}\text{S}_{\text{pyrite}}$ signals have been commonly interpreted to record the signature of syndepositional MSR and have thus been used for local and/or global paleoenvironmental reconstructions (e.g., Chen et al., 2013; Sim et al., 2015; Wang et al., 1996). However,

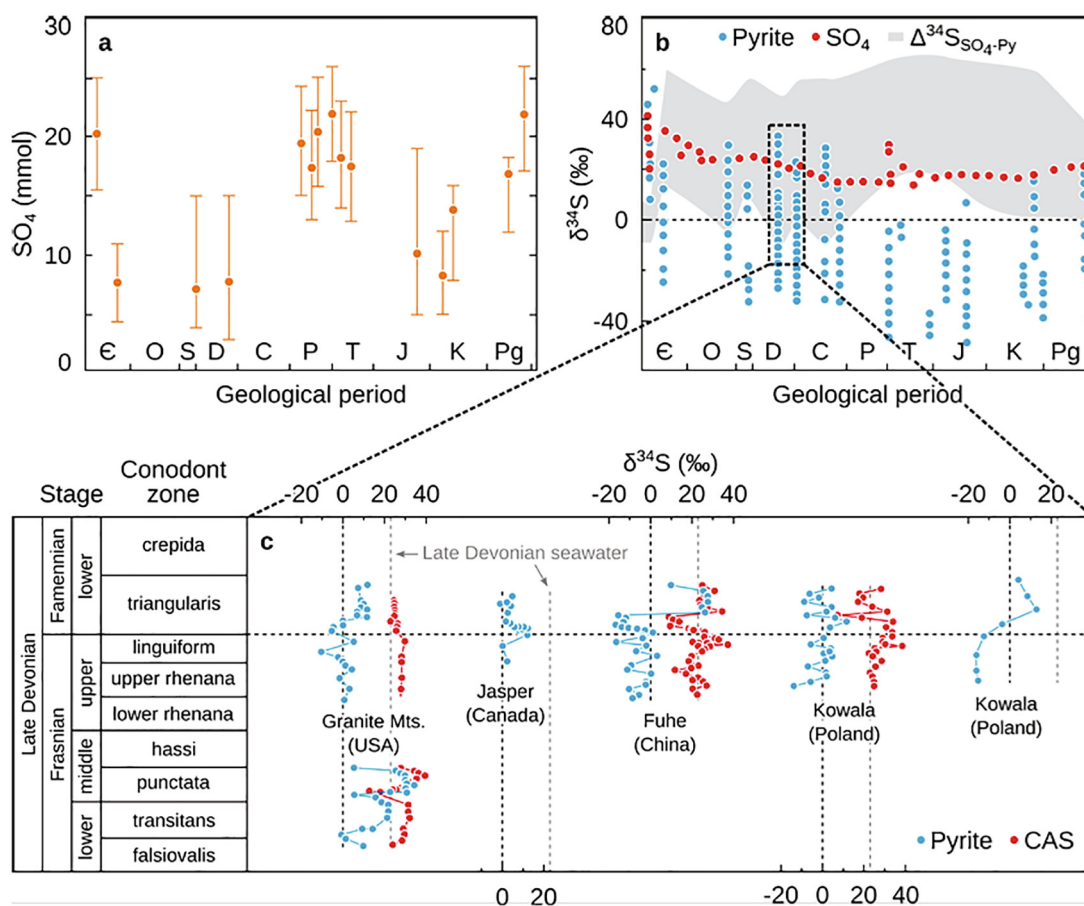


Fig. 1. (a) Estimates of Phanerozoic seawater sulfate concentrations based on fluid inclusion data from marine evaporates (modified from Fike et al., 2015). (b) The sulfur isotope record of Phanerozoic sedimentary pyrite (blue circles) and sulfates (red circles; modified from Fike et al., 2015). The shaded area indicates the envelope of observed sulfur isotope fractionations between sedimentary sulfate and pyrite ($\Delta^{34}\text{S}_{\text{sulfate-pyrite}}$). (c) The sulfur isotope record of pyrite and carbonate-associated sulfate (CAS) in Late Devonian sedimentary carbonate rocks from the Granite Mountains, USA (Sim et al., 2015); Jasper, Canada (Geldsetzer et al., 1987; Goodfellow and Jonasson, 1984; Wang et al., 1996); Fuhe, China (Chen et al., 2013); and Kowala, Poland (Chen et al., 2013; Joachimski et al., 2001). The Late Devonian is characterized by a strikingly positive excursion in pyrite sulfur isotope ratios, which are variable in their timing, duration, and magnitude. Some pyrites from that time display extremely positive $\delta^{34}\text{S}$ values, even higher than that of the inferred Late Devonian seawater sulfate (i.e., $\delta^{34}\text{S}_{\text{pyrite}} > \delta^{34}\text{S}_{\text{sulfate}}$; $\delta^{34}\text{S}_{\text{sulfate}} = \sim +23\text{‰}$; gray dashed line), as reconstructed from CAS in the calcite lattice (Kampschulte and Strauss, 2004).

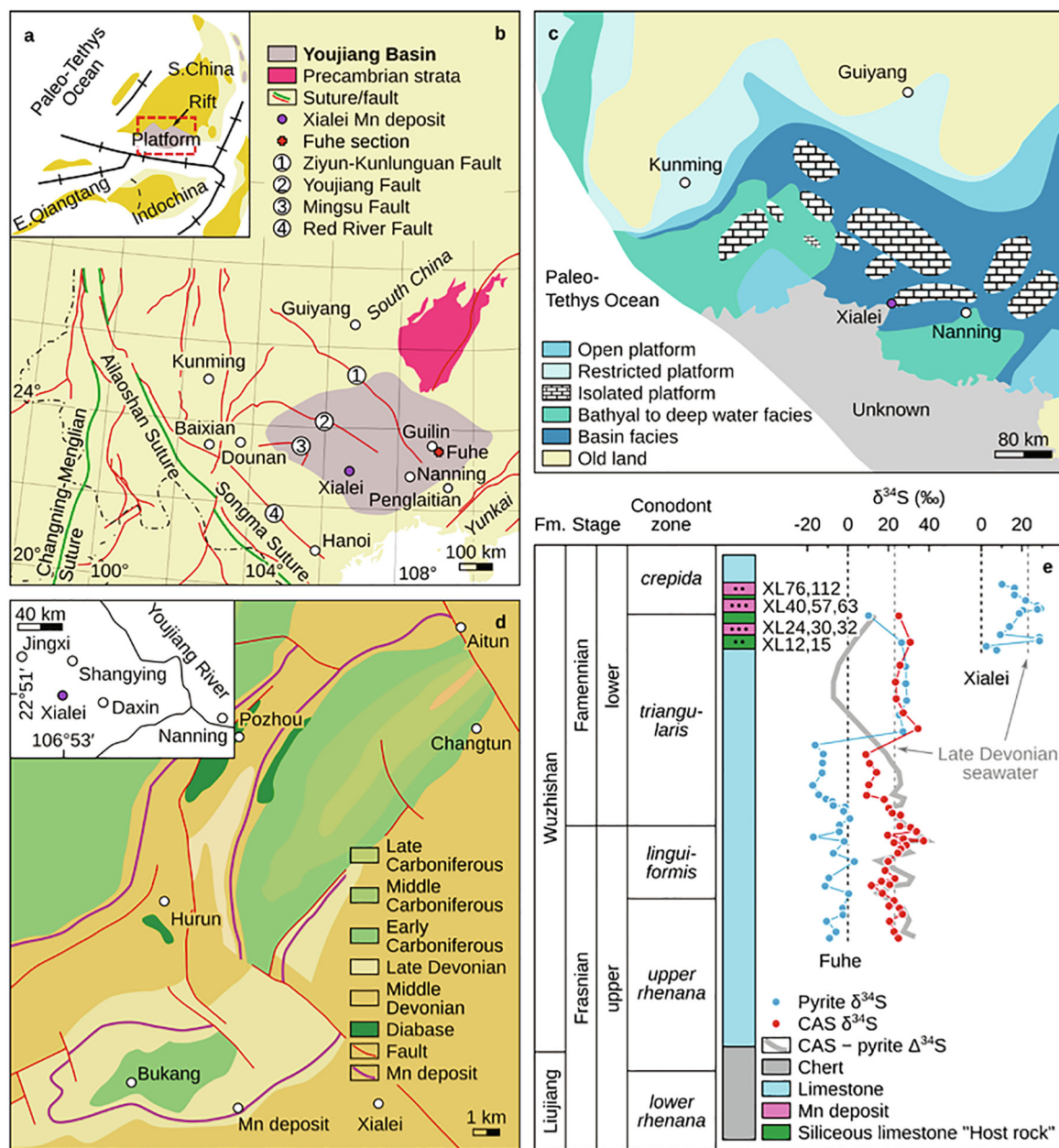


Fig. 2. (a) Geodynamic models of Late Devonian Mn mineralization in the southwestern South China Block (SCB) in the context of Paleo-Tethys evolution. Red rectangle indicates the location of the studied region (modified from Chen et al., 2018). (b) Simplified geological map showing the distribution of Late Devonian sedimentary Mn deposits in the southwestern SCB (Chen et al., 2018). Gray area indicates the Youjiang Basin; purple circle indicates the location of the studied Xialei mine in Daxin County, Guangxi Province; and red polygon indicates the lower Famennian Fuhe section that was found to contain ^{34}S -enriched pyrite (Chen et al., 2013). (c) Late Devonian palaeogeography of the southwestern SCB. The lithological associations in the depositional facies are explained as follows. Open platform: limestone, marlstone and packstone; restricted platform: marlstone-dolomite, dolomite and limestone; isolated platform: biogenic-bioherm limestone and dolomite; bathyal-deep sea facies: chert, deep-sea chert and mudstone; and basin facies (B): argillaceous limestone, chert, shale and limestone. Revised from BGMRG (Bureau of Geology and Mineral Resources of Guangxi Zhuang Autonomous Region) (1985); Chen et al. (2018). (d) Geological sketch map of the Xialei Mn deposit (revised from Zeng and Liu, 1999), inset shows the immediate geographical location within Guangxi province. (e) Stratigraphy of the Xialei Mn deposit among the Late Devonian strata, Youjiang Basin. Black dots on the stratigraphic column indicate sample locations. Lithology and conodont zones adapted from Huang et al. (2018); Li (2007); Ma et al. (2016); Song et al. (2018) and Zeng and Liu (1999). Bulk-rock sulfur isotope values of pyrite and carbonate-associated sulfate (CAS), and related $\Delta^{34}\text{S}_{\text{CAS-pyrite}}$ data from the Fuhe section of the Youjiang Basin are from Chen et al. (2013), and bulk-rock sulfur isotope values of pyrite in the Xialei Mn deposit, Youjiang Basin are from Qin et al. (2010). There are some anomalously positive $\delta^{34}\text{S}_{\text{pyrite}}$ values, many of which are higher than the contemporaneous seawater $\delta^{34}\text{S}_{\text{sulfate}}$ values (gray dashed line). (For interpretation of the references to colour in this figure legend, the reader is referred to the web version of this article.)

the previous studies have all relied on traditional bulk-rock analysis so that values reported may average over pyrites generated from a broad spectrum of processes from syndepositional to postdepositional.

The Wuzhishan Formation in South China provides an ideal location to revisit the genesis of these pyrites. The Wuzhishan Formation is upper Frasnian to Famennian in age and mainly contains banded lenticular limestone with a sediment-hosted Mn deposit between the Late *triangularis* and *crepida* conodont zones of the lower Famennian (e.g., the Xialei deposits; Fig. 2e; Huang et al., 2018; Li, 2007; Ma et al., 2016; Song et al., 2018). Chen et al. (2013) documented a positive excursion in bulk-rock $\delta^{34}\text{S}_{\text{pyrite}}$ coupled with a negative effective isotope fractionation between pyrite and coexisting carbonate-associated sulfate CAS ($\Delta^{34}\text{S}_{\text{CAS-pyrite}} = \delta^{34}\text{S}_{\text{CAS}} - \delta^{34}\text{S}_{\text{pyrite}}$) in the Late *triangularis* conodont zone of the Fuhe Mn deposit (Fig. 2e), whereas Qin et al. (2010) and Zeng and Liu (1999) found $\delta^{34}\text{S}_{\text{pyrite}}$ values approaching or exceeding that of coeval seawater ($\delta^{34}\text{S}_{\text{sulfate}} = \sim +23\%$; reconstructed from CAS in the calcite lattice; Kampschulte and Strauss, 2004) in the correlative Xialei Mn deposit, Daxin location. Aiming to unravel the genetic mechanism of these Late-Devonian positive $\delta^{34}\text{S}_{\text{pyrite}}$ signals in South China, and to further explore its relationship to both the local and global sulfur cycles, here we carried out detailed petrographic observations using scanning electron microscopy (SEM) and in-situ micrometer-scale $\delta^{34}\text{S}_{\text{pyrite}}$ analysis via multi-collector inductively coupled plasma mass spectrometry (MC-ICP-MS) on the pyrite samples from the Xialei Mn deposit.

2. GEOLOGICAL SETTING

2.1. Regional geology and palaeogeography

The evolution of the Palaeo-Tethys Ocean played an important role in Paleozoic tectono-metallogenesis in Southeast Asia, where several crustal blocks were amalgamated during the closure of this paleo-ocean (Fig. 2a; Deng and Wang, 2016; Metcalfe, 2006). The South China Block (SCB) was separated by the Jinshajiang, Ailaoshan, and Songma sutures from other Palaeo-Tethyan blocks, including the Indochina, Eastern Qiangtang, and Western Qiangtang blocks. The Youjiang Basin covers most of the southwestern SCB and extends from southwestern China to northeastern Vietnam (Fig. 2b; Yang et al., 2012). In addition to a significant amount of endogenic metallogenesis, there are several economically significant Late Devonian sedimentary Mn deposits in the Youjiang Basin, including the Xialei Mn deposit. The formation of these Mn deposits has been proposed to reflect an initial response to the opening of the Palaeo-Tethys Ocean (Chen et al., 2018).

The paleogeographic reconstruction and description of sedimentary facies has been detailed in previous studies (Chen et al., 1994; Chen et al., 2018; Chen and Shi, 2006; Du et al., 2013; Ma et al., 2016). Deep water sediments, such as a radiolarian chert, indicate that the Youjiang Basin was a rift environment in the Early to Middle Devonian (Chen et al., 2018; Chen and Shi, 2006), and that a

large-scale regression occurred in the Late Devonian (Du et al., 2013; Ma et al., 2016; Zeng et al., 1993). Evidence of Devonian volcanism recorded in the SCB is linked to syndepositional intraplate rifting (Du et al., 2013). In the Late Devonian, the Youjiang Basin was dominated by isolated carbonate platforms scattered across a wide basin (Fig. 2c; Huang et al., 2018; Ma et al., 2009; Song et al., 2018). These isolated platforms consist of both limestone and dolostone and contain abundant bioherms (Chen et al., 2013; Ma et al., 2009). The remainder of the basin was filled with argillaceous limestone, chert and shale. The latter may represent a true deep sea (>1 km) depositional environment (Chen et al., 2018). Manganese ore deposits occur along the margins of the basin and are mainly located along the transitional zones between uplift and local depressions in the Youjiang Basin.

2.2. Deposit description

The Late Devonian rocks of the Youjiang Basin, exposed in southwestern Guangxi Province, are Mn-rich on a regional scale (Fig. 2d). Rocks exposed in the Xialei Mn deposit have been divided into the Liujiang and the overlying Wuzhishan formations, which are Frasnian (382.7–372.2 Ma) to Famennian (372.2–358.9 Ma) in age (Fig. 2e; Huang et al., 2018; Ma et al., 2009; Qin et al., 2010; Song et al., 2018; Zeng and Liu, 1999). The boundary between the Wuzhishan Formation and the Liujiang Formation is located at the base of the Upper *rhenana* conodont zone, corresponding to the upper Frasnian (Fig. 2e; Huang et al., 2018; Song et al., 2018). The underlying Liujiang Formation varies between 47 and 234 m in thickness and consists mainly of chert intercalated with micritic limestone (Huang et al., 2018; Song et al., 2018; Zeng and Liu, 1999). The Wuzhishan Formation has been further divided into four members by Cong et al. (2018), and is characterized by banded lenticular limestones intercalated with calcareous mudstone and argillaceous limestone (Chen et al., 2018; Qin et al., 2010; Zeng and Liu, 1999).

The Xialei Mn deposits are hosted in the second member of the Wuzhishan Formation. The anomalous Mn enrichment in the Late Devonian strata of the Youjiang Basin (Ma et al., 2016) and the presence of the conodont *Palmatolepis* min. *minuta* in the Xialei Mn deposit (Li, 2007) indicate that the Xialei Mn deposit is hosted in strata that span the Late *triangularis* through *crepida* conodont zones, indicating a lower Famennian age (Fig. 2e). This correlates with the positive $\delta^{34}\text{S}_{\text{pyrite}}$ excursion and negative $\Delta^{34}\text{S}_{\text{CAS-pyrite}}$ constrained in the Late *triangularis* conodont zone within the Fuhe region of the Late Devonian Youjiang Basin (Fig. 2e; Chen et al., 2013). The ore-bearing section is ~ 20 m thick and composed of three distinct horizons separated by layers of chert and siliceous limestone. The mineral assemblage of the Mn ores is dominated by early diagenetic Mn(II)-carbonates, with minor Mn(II)-silicates. Magnetite and pyrite have also been documented within the ores. The ores have a microcrystalline texture and occur as thin, parallel or wavy beds and laminae, which are cross-cut by later stage high-temperature rhodonite veins (e.g., Zeng and Liu, 1999). Laminated textures reflect syndepositional

processes, while the cross-cutting veins indicate the existence of secondary hydrothermal fluids which partially altered the earlier Mn-carbonate to rhodonite.

3. SAMPLES AND METHODS

3.1. Sample description

A total of ten samples were collected from the Xialei Mn ore mining district (22°54'29"N, 106°42'24"E), Daxin County, Guangxi Province, South China. The Xialei mine is the largest known Mn ore reserve in China. Two samples, XL-12 and XL-15, are from the underlying siliceous limestone at the foot of the Mn ores and are referred to as the host rocks hereafter. Three samples (XL-24, XL-30, and XL-32) are from the first ore horizon, three (XL-40, XL-57, and XL-63) from the second horizon, and two (XL-76 and XL-112) from the third horizon (Fig. 2e). Individual pyrite grains were imaged by optical and scanning electron microscopy (SEM) at the State Key Laboratory of Geological Processes and Mineral Resources (GPMR), China University of Geosciences (Wuhan). Backscattered electron microscopy (BSE) images of carbon-coated samples were acquired with a field emission scanning electron microscope (FESEM), JEOL JXA-8100, and a JSM-35CF high definition backscatter electron detector (HDBSD), respectively.

3.2. EPMA analysis

Mineral compositions were determined at the GPMR lab, China University of Geosciences (Wuhan), on a JEOL JXA-8100 Electron Probe Micro-Analyzer (EPMA) equipped with four wavelength-dispersive spectrometers (WDS). Samples were coated with a thin conductive carbon film prior to analysis. The methods of Zhang and Yang (2016) were used to minimize the difference in carbon film thickness between samples and obtain a ~20 nm uniform coating. During the analysis, an accelerating voltage of 15 kV, a beam current of 20 nA, and a 1 μm spot size were used. Data were corrected on-line using a modified ZAF (atomic number, absorption, fluorescence) correction procedure. The peak counting time was 10 s for Na, Mg, Al, Si, K, Ca, Fe and 20 s for Ti and Mn. The background counting time was one-half of the peak counting time on the high- and low-energy background positions. Standards used included sanidine (for K), pyrope garnet (for Fe and Al), diopside (for Ca and Mg), jadeite (for Na), rhodonite (for Mn), olivine (for Si), and rutile (for Ti). The EMPA was also used to map specific elements within the complex matrices of samples, complementing the sedimentological relationships observed microscopically. During the analysis, an accelerating voltage of 15 kV, a beam current of 50 nA, and a 1 μm spot size were used, along with a dwell time of 60 ms.

3.3. In-situ sulfur isotope analysis

Sulfur isotope analysis was carried out on sulfides from standard polished sections using a Nu Plasma II

multi-collector inductively coupled plasma mass spectrometer (MC-ICP-MS) system, equipped with a RESOLUTION S-155 193 nm ArF excimer laser ablation system at the GPMR lab, China University of Geosciences (Wuhan). During the experiment, the diameter of the laser spot was 33 μm with a laser repetition rate of 10 Hz, and the ablation process was set to last for 40 s. Standard-sample bracketing (SSB) was used to determine the $\delta^{34}\text{S}$ ($\delta^{34}\text{S} = ({}^{34}\text{S}/{}^{32}\text{S})_{\text{sample}} / ({}^{34}\text{S}/{}^{32}\text{S})_{\text{VCDT}} - 1$) values of the samples throughout the MC-ICP-MS analytical sessions. An international sphalerite standard NBS-123 ($\delta^{34}\text{S}_{\text{VCDT}} = +17.1\%$) and an in-house pyrite standard named WS-1, a natural pyrite crystal from the Wenshan polymetallic skarn deposit in Yunnan Province in South China, were used to calibrate the mass bias for sulfur isotopes. The $\delta^{34}\text{S}_{\text{VCDT}}$ values ($+1.1\% \pm 0.2\%$) of WS-1 were determined by secondary ion mass spectrometry (SIMS) at the Chinese Academy of Geochemistry, Guangzhou (Zhu et al., 2016). The sulfur isotopic ratios of samples were corrected for instrumental mass bias based on linear interpolation between two neighboring standards. The 2σ analytical error is estimated to be $\pm 0.3\%$.

4. RESULTS

4.1. Petrographic characterization of pyrite and paragenetic minerals

The host rocks of the Xialei Mn-containing ores (e.g., samples XL-12 and XL-15) contain pyrites characterized by relatively poor inclusions and euhedral-subhedral habits (Fig. 3a–d), with carbonate as the main mineral in the matrix. Recrystallized carbonate occurs along the rims of the subhedral pyrites in sample XL-12 (Fig. 3a and b). Voluminous magnetite grains containing carbonate inclusions surround the pyrites in sample XL-15 (Fig. 3d).

In the Xialei Mn-containing ores, the main matrix components that contain Mn are Mn(II)-carbonate and Mn(II)-silicate. Magnetite grains (Table 1) are found in some samples, generally as two distinct textures, including banded (Fig. 3e) and disseminated grains (Fig. 3f). Additionally, magnetite may have a lacy (Figs. 4c, j, l, 5e, 6g), grainy (Fig. 4e, g, h) or residual (Fig. 4k) texture. Lacy magnetite cements are observed to have surrounded the pyrite grains, while a residual texture is characteristic of pyrites that replace and inherit the crystal habit of a precursor magnetite. Both types of magnetite contain Mn(II)-carbonate inclusions (e.g., Fig. 4e, k). Based on the paragenetic relationship between the Mn minerals and magnetite, pyrite phases in the Xialei Mn ores can be broadly divided into three types: (Type I) inclusion-rich pyrite, (Type II) overgrowth pyrite, and (Type III) inclusion-poor, mainly subhedral pyrite grains. All three types are described in detail below for each sample.

In samples XL-24 and XL-30, all three types of pyrite are present (Fig. 4). Type I pyrites show disseminated textures and are subhedral to anhedral in habit (Fig. 4g–i). These pyrites also contain Mn(II)-carbonates as inclusions (Fig. 4a–d, f) and are surrounded by Type II pyrites (Fig. 4a–d, f–g). There also appears to be a mutually

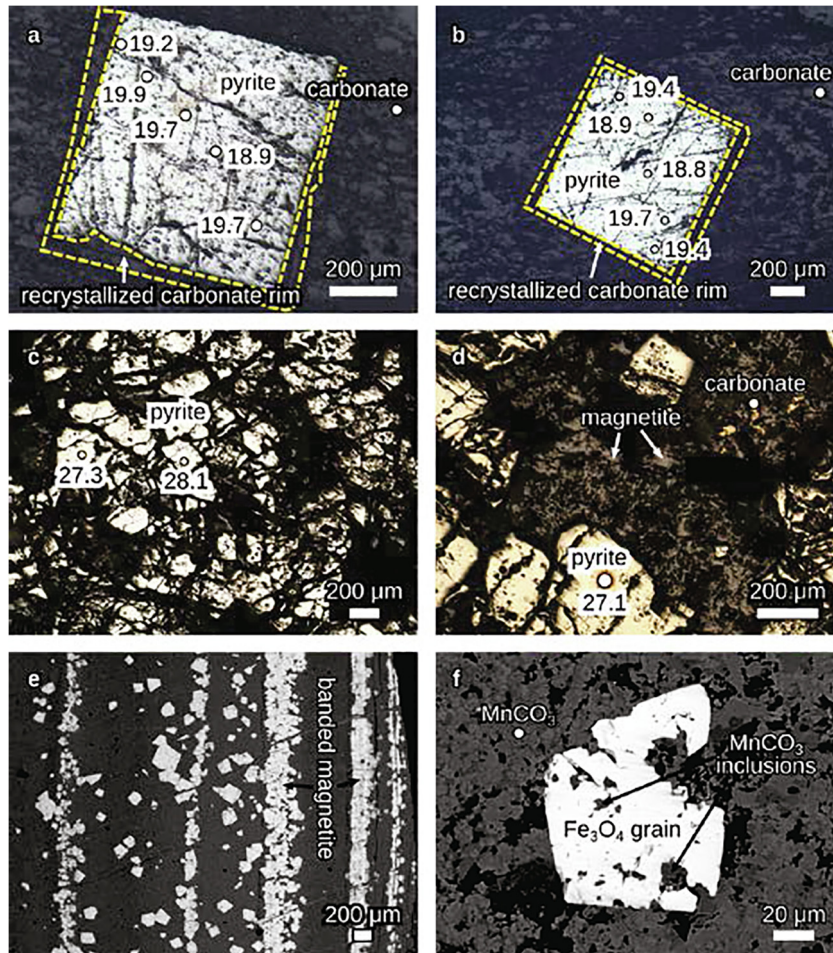


Fig. 3. (a–d) Optical micrographs of the siliceous limestone (host rock) samples XL-12 (a, b) and XL-15 (c, d). The matrix is carbonate. Laser ablation scars where in-situ $\delta^{34}\text{S}_{\text{pyrite}}$ measurements were made are shown as white circles with numbers. $\delta^{34}\text{S}_{\text{pyrite}}$ values are positive and homogeneous within each sample. Euhedral pyrites are surrounded by recrystallized carbonate (a and b; yellow dashed lines). Subhedral pyrites are surrounded by magnetite (d). (e–f) Backscattered electron (BSE) micrographs of magnetite in the Xiaiei Mn deposit. They include banded magnetite (e) and disseminated magnetite grains locally containing Mn-carbonate inclusions (f). The matrix is mainly Mn-carbonate. (For interpretation of the references to colour in this figure legend, the reader is referred to the web version of this article.)

replaceable relationship between Type I pyrite and grainy magnetite (Fig. 4e, g–i). In contrast, Type II pyrites generally display an overgrowth habit and only rarely contain Mn(II)-carbonate inclusions (Fig. 4a–d, f–g). Type III pyrites are distinguished from Type I in having less amounts of inclusions and from Type II in occurring in a disseminated manner. In samples XL-24 and XL-30, they are largely devoid of Mn(II)-carbonate inclusions, and appear to inherit the crystal habit of a precursor magnetite (Fig. 4k) or be surrounded by lacy magnetite (Fig. 4c, j, l). Noticeably, recrystallized Mn(II)-carbonates are observed along the rims of both Type II (Fig. 4c, f) and Type III pyrite (Fig. 4j–l), and also separate the Type III pyrites from the lacy and residual magnetite (Fig. 4j–l). Furthermore, Electron probe micro-analysis (EPMA) maps of relative O, S, and Fe content (Fig. 5b–d, f–h) further show the similarity between Type III pyrites (inclusion-poor pyrite) and magnetite.

In sample XL-32, only one type of pyrite is observed – Type III (Fig. 6a–c). Although the grains contain relatively abundant Mn(II)-carbonate inclusions, the total amount is less than that seen in the Type I pyrites observed in samples XL-24 and XL-30. The affinity of the grains to Type III is further evident based on the following four characteristics. First, the pyrite grains in sample XL-32 are subhedral to euhedral in shape, and unlike Type I pyrite in samples XL-24 and 30 (Fig. 4e, g–h), there is no indication of corrosion or dissolution along the edges. Second, no Type II pyrite appears to have overgrown these grains. Third, recrystallized Mn(II)-carbonate occurs along the rim of these pyrites (Fig. 6b). Finally, some ZnS minerals occur along the rims or as inclusions in these pyrite grains (Fig. 6b and c), which is similar to Type III pyrite in several other samples described below.

In samples XL-40, -57, -63, -76 and -112, no Type I pyrite was observed. Type III pyrite occurs only as

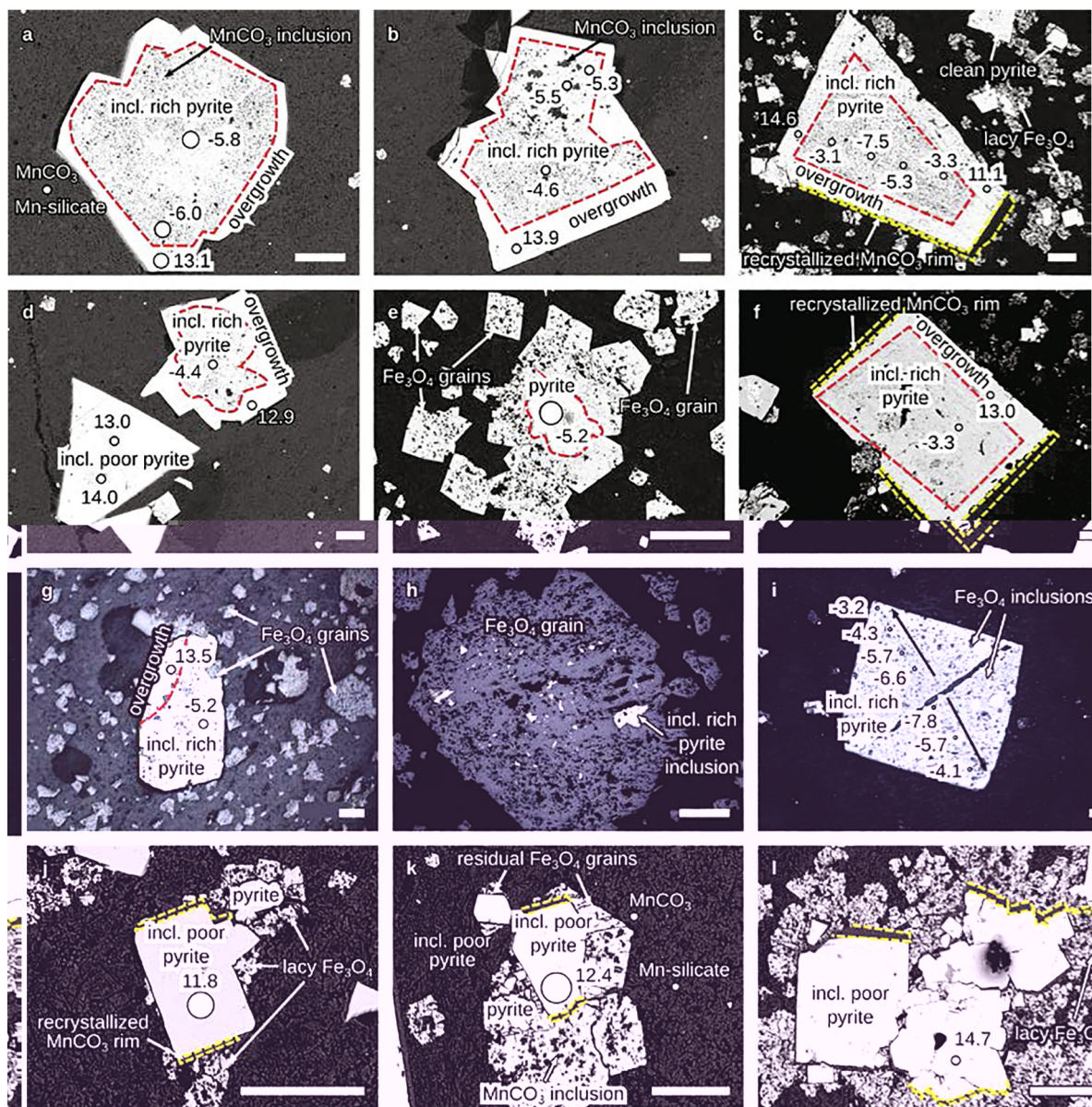


Fig. 4. BSE (a–f, j–l) and optical (g–i) micrographs showing laser ablation scars of in-situ $\delta^{34}\text{S}_{\text{pyrite}}$ measurements (white circles with numbers) of Mn ore samples XL-24 (a, e, g–k) and XL-30 (b–d, f, l). The matrix is Mn-carbonate and Mn-silicate. Magnetite (Fe_3O_4) occurs with lacy (c, j, l), grainy (e, g, h), and residual (k) textures; all contain Mn-carbonate inclusions. Inclusion (abbreviated as incl.)-rich pyrites and magnetite grains appear in a mutually replaceable relationship (e, g–i). Inclusion-rich pyrite also contains Mn-carbonates as inclusions (a–d, f) and is surrounded by overgrowth pyrites (a–d, f–g). The inclusion-poor pyrite grains are surrounded by lacy magnetite (c, j, l) and inherited the crystal habit of magnetite grains (k). Noticeably, recrystallized Mn-carbonate rims (yellow dashed lines) separate the inclusion-poor pyrite from the magnetite (j–l). Red dashed lines are the boundary between inclusion-rich and overgrowth pyrite (a–g). The overgrowth pyrites are also surrounded by the recrystallized Mn-carbonate rims (yellow dashed lines) (c, f). $\delta^{34}\text{S}_{\text{pyrite}}$ values of inclusion-rich pyrites are low, even negative (a–g), and gradually increase from the core to the edges (black arrows, i), while overgrowth pyrites and inclusion-poor pyrites display higher, positive, and more uniform values (a–d, f–g, j–l). Scale bars represent 100 μm . (For interpretation of the references to colour in this figure legend, the reader is referred to the web version of this article.)

disseminated, subhedral to euhedral grains, and is generally less inclusion-rich than in sample XL-32 (Fig. 6d–o). Recrystallized Mn(II)-carbonate rims commonly surround these pyrite grains (Fig. 6b, j), and ZnS minerals are present as inclusions inside several pyrite grains in samples XL-57 and XL-112 (Fig. 6g–i, n). Lacy magnetite grains may also be present around the pyrite grain (Fig. 6g). In addition,

“flower-shaped” pyrite is noted to occur in sample XL-76 (Fig. 6l).

4.2. Sulfur isotope compositions

The sulfur isotope data for the pyrite standard WS-1 and each type of pyrite identified above are provided in

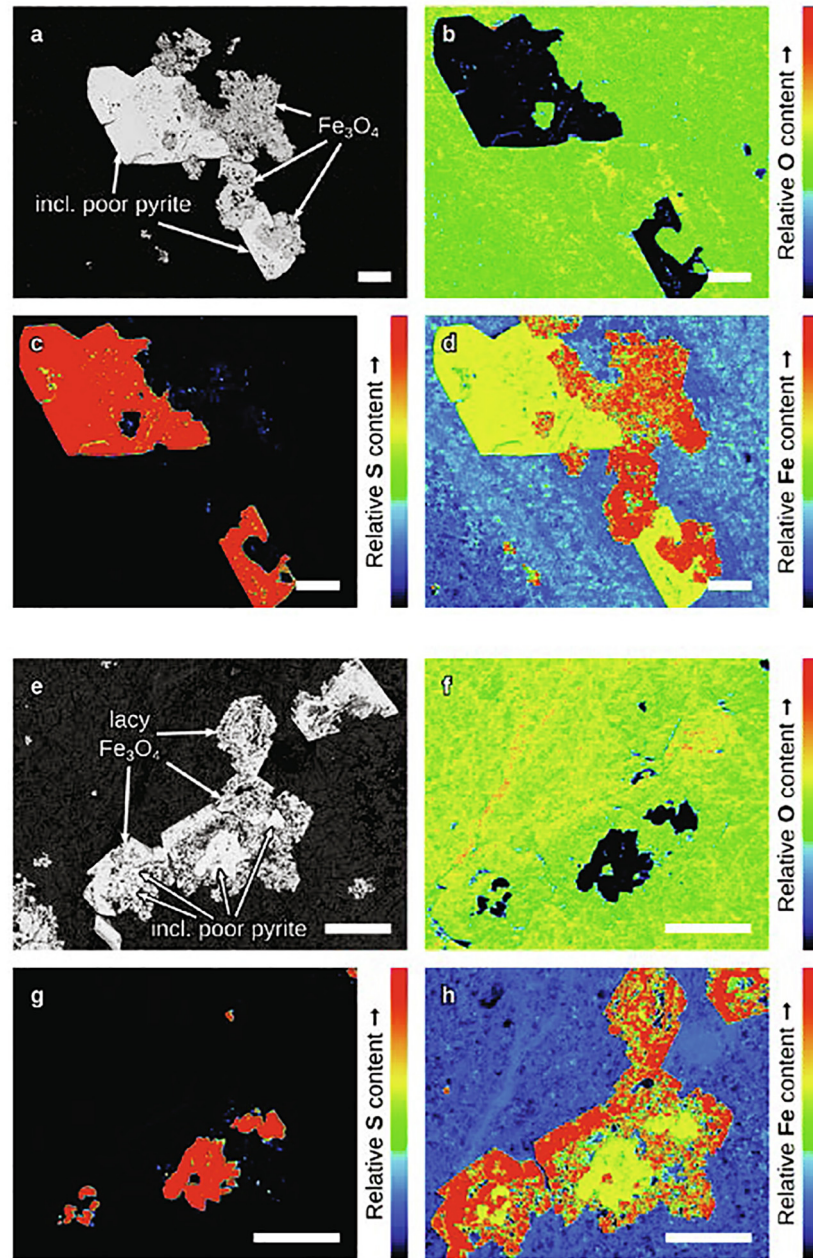


Fig. 5. BSE micrographs of Mn ore sample XL-24 (a) and XL-30 (e) showing the replaceable relationship between inclusion (abbreviated as incl.)-poor pyrite and magnetite. Electron probe micro- analysis (EPMA) maps show relative O, S, and Fe content, respectively (b–d, f–h). Scale bars represent 100 μm .

Table 2 and Fig. 7. In host rock samples XL-12 and XL-15, the $\delta^{34}\text{S}$ values are relatively homogeneous, from +18.1‰ to +20.0‰ and +26.5‰ to +28.1‰, respectively. In Sample XL-24 and XL-30, which contain all three types of pyrites, a bimodal distribution of $\delta^{34}\text{S}_{\text{pyrite}}$ values was observed. Type I (inclusion-rich) pyrites are characterized by a narrow range of negative $\delta^{34}\text{S}_{\text{pyrite}}$ values from -7.3‰ to -2.0‰ . In contrast, both Type II and Type III pyrites show positive $\delta^{34}\text{S}$ values that are relatively homogeneous within a sample but vary in a large extent between

samples. Across samples XL-32, -40, -76 and -112, Type III pyrites have a $\delta^{34}\text{S}$ range from +4.2‰ to +37.6‰. Notably, micrometer-scale $\delta^{34}\text{S}_{\text{pyrite}}$ analysis reveals small in-grain variations: in particular, a consistently decreasing trend from the core to the edges of individual pyrite grains in Sample XL-40 (Fig. 6d–f). The $\delta^{34}\text{S}$ values of Type III pyrites increase to $\sim+17\text{‰}$ (Fig. 6h–i), similar to the values ($\sim+18\text{‰}$) of the paragenetic ZnS mineral in sample XL-57 (Fig. 6i), and even reach values as high as $\sim+37.6\text{‰}$ in sample XL-63 (Fig. 6j).

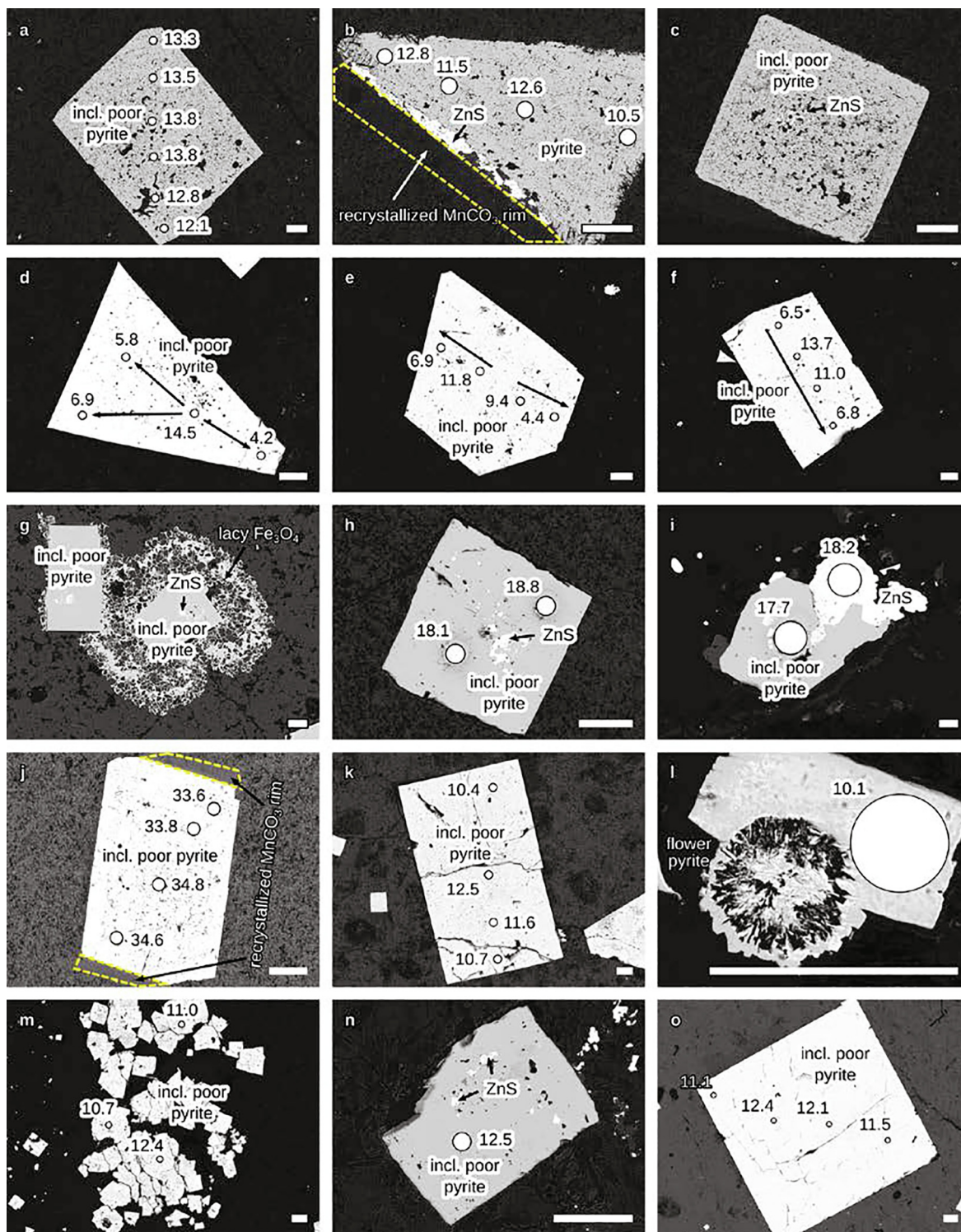


Fig. 6. Backscattered electron (BSE) micrographs showing laser ablation scars of in-situ $\delta^{34}\text{S}_{\text{pyrite}}$ measurements (white circles with numbers) of Mn ore samples XL-32 (a–c), XL-40 (d–f), XL-57 (g–i), XL-63 (j), XL-76 (k–m), and XL-112 (n–o). The matrix is Mn-carbonate and Mn-silicate. Subhedral- euhedral inclusion (abbreviated as incl.)-poor pyrite grains contain some few Mn-carbonate (a, c) and ZnS inclusions (c, g–i, n), and are surrounded by recrystallized Mn-carbonate rims (yellow dashed lines, b, j) and ZnS (b). Lacy magnetite surrounds the euhedral inclusion-poor pyrite (g). An example of a flower pyrite is shown in panel (l). In sample XL-40, $\delta^{34}\text{S}_{\text{pyrite}}$ data displays a decreasing trend from the core to the edges of individual pyrite grains (black arrows, d–f). Sample XL-63 hosts extremely positive $\delta^{34}\text{S}$ ratios compared to other samples and contemporaneous seawater $\delta^{34}\text{S}_{\text{sulfate}}$ (j). Scale bars represent 100 μm . (For interpretation of the references to colour in this figure legend, the reader is referred to the web version of this article.)

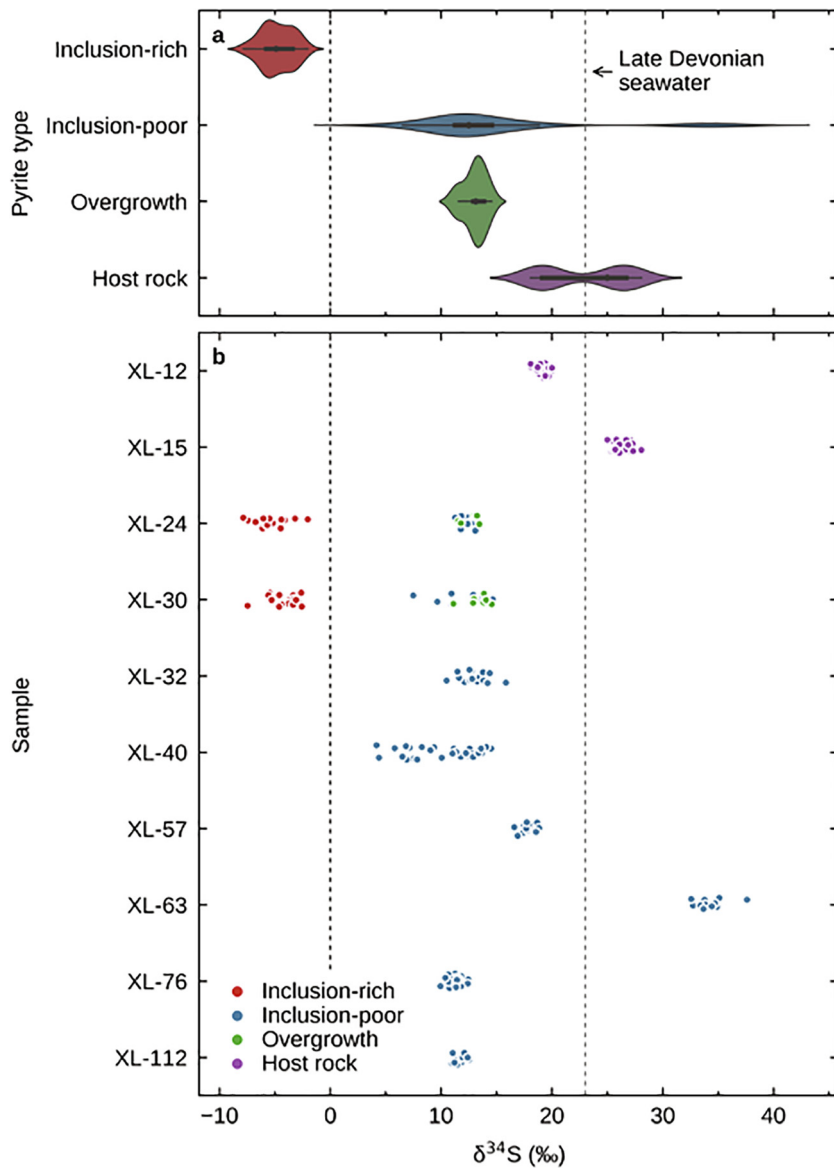


Fig. 7. Violin plots (with box plot insets) and scattered data of the in-situ MC-ICP-MS $\delta^{34}\text{S}$ measurements in this study. Different textures show distinct ranges of $\delta^{34}\text{S}_{\text{pyrite}}$. Right dashed line represents the Late Devonian seawater $\delta^{34}\text{S}_{\text{sulfate}}$ value (Kampschulte and Strauss, 2004). Note the relatively large range of $\delta^{34}\text{S}$ data measured from XL-24 and XL-30; homogeneous $\delta^{34}\text{S}$ values measured from XL-12, -15, -32, -40, -57, -63, -76 and -112; and remarkably positive $\delta^{34}\text{S}_{\text{pyrite}}$ values measured from XL-15 and -63 that exceed contemporaneous Late Devonian seawater. See the main text for detailed discussion of these patterns and their interpreted origins.

5. DISCUSSION

5.1. Previous models for the Late Devonian positive $\delta^{34}\text{S}_{\text{pyrite}}$ excursions in South China

The Wuzhishan Formation in the Youjiang basin, South China, exemplifies the need to consider local controls on the Late Devonian $\delta^{34}\text{S}_{\text{pyrite}}$ excursion. In particular, the Fuhe section is characterized by a markedly higher magnitude in $\delta^{34}\text{S}_{\text{pyrite}}$, up to +27‰, compared with the average global values for the excursion (<+20‰; Fig. 1c), suggesting that local depositional environments played an important role in modulating its expression (Chen et al., 2013). To explain

these values, previous studies have leveraged basinal influences on MSR.

Based on a comparison between $\delta^{34}\text{S}_{\text{pyrite}}$ and contemporaneous seawater $\delta^{34}\text{S}_{\text{sulfate}}$ ($\delta^{34}\text{S}_{\text{sulfate}} = \sim +23\text{‰}$; Kampschulte and Strauss, 2004), pyrites with a positive $\delta^{34}\text{S}_{\text{pyrite}}$ excursion in the Fuhe section are divided into two types: (1) $\Delta^{34}\text{S}_{\text{sulfate-pyrite}} > 0$ and (2) $\Delta^{34}\text{S}_{\text{sulfate-pyrite}} < 0$. In the first case, the positive $\delta^{34}\text{S}_{\text{pyrite}}$ excursion coupled with diminished $\Delta^{34}\text{S}_{\text{sulfate-pyrite}}$ has been attributed to a basinal drop in sulfate availability – experimental studies suggest that lower sulfate concentrations could cause smaller $\Delta^{34}\text{S}_{\text{sulfate-sulfide}}$ and more positive $\delta^{34}\text{S}_{\text{pyrite}}$ values during MSR (Habicht et al., 2002). The

restricted hydrography of the Youjiang Basin could have limited the lateral water circulation with the already sulfate-depleted Late Devonian Ocean. This could have further intensified the intrabasinal sulfate depletion, so that $\delta^{34}\text{S}_{\text{pyrite}}$ evolved to near seawater $\delta^{34}\text{S}_{\text{sulfate}}$ values (Chen et al., 2013). However, the contemporary seawater sulfate concentrations, estimated from fluid inclusions in evaporate, could have approached about 7 mM (Lowenstein et al., 2003), less than that of the modern ocean (28 mM), but still at least an order of magnitude higher than the experimentally-determined threshold (<200 μM) for depressed sulfur isotope fractionation during MSR (Habicht et al., 2002; Habicht and Canfield, 2001; Horita et al., 2002). In addition, a more recent study on Lake Matano (Indonesia) suggests that large fractionations (>20‰) persist at sulfate levels below 20 μM (Crowe et al., 2014). Therefore, sulfate limitation in the Youjiang basin appears to be an insufficient explanation for the high $\delta^{34}\text{S}$ values of the Late Devonian pyrites in South China.

The second case, the occurrence of negative $\Delta^{34}\text{S}_{\text{sulfate-pyrite}}$ values, is even more puzzling: during MSR, $\delta^{34}\text{S}_{\text{pyrite}}$ can approach, but cannot exceed, the coexisting $\delta^{34}\text{S}_{\text{sulfate}}$ signal even as the seawater sulphate concentration declines substantially (Böttcher, 2011; Canfield, 2001a; Kaplan and Rafer, 1958; Kaplan and Rittenberg, 1964). However, abiotic sulfide oxidation, in which hydrogen sulfide or sulfide minerals produced through MSR are converted to oxidized sulfur species (e.g., sulfate), could explain these values. Laboratory experiments have shown that the abiotic oxidation of H_2S by O_2 has a kinetic fractionation of 4‰–5‰, resulting in an increase in $\delta^{34}\text{S}$ of the residual H_2S pool (Fry et al., 1988). This mechanism would allow for the generation of $\delta^{34}\text{S}_{\text{pyrite}}$ values enriched relative to seawater sulfate (e.g., Ries et al., 2009). Therefore, Chen et al. (2013) proposed that the negative $\Delta^{34}\text{S}_{\text{sulfate-pyrite}}$ was caused by intense aerobic reoxidation of dissolved sulfide in low sulfate waters, which might be driven by a coeval, rapid oxygenation event on the basin floor. This process may have occurred during the sea level lowstand in the local depositional environment caused by the Gondwana glaciation (Isaacson et al., 2008). The potential for sea level changes to affect $\Delta^{34}\text{S}_{\text{sulfate-pyrite}}$ in local stratigraphic sections is supported by $\delta^{34}\text{S}_{\text{pyrite}}$ values in excess of seawater sulfate in modern shallow water environments and elsewhere that are associated with oxidative sedimentary reworking during early diagenesis (e.g., Aller et al., 2010; Gao et al., 2013; Hints et al., 2014; Ries et al., 2009; Rose et al., 2019). This inference is strengthened in the Fuhe section by a positive $\delta^{34}\text{S}_{\text{CAS}}$ excursion to values heavier than those anticipated for seawater sulfate (Kampschulte and Strauss, 2004), and a transient decrease in $\delta^{34}\text{S}_{\text{CAS}}$ by $\sim 10\%$. These abrupt isotope changes in CAS could have resulted from the enhanced closed-system conditions, likely associated with increased sedimentation rate during sea level as discussed in the recent studies of Richardson et al. (2019a,b). However, these previous models are based on bulk $\delta^{34}\text{S}_{\text{pyrite}}$ analyses and assume that MSR is the dominant mechanism. A reappraisal leveraging in-situ analysis on individual grains will enable us to determine whether the Late Devonian $\delta^{34}\text{S}_{\text{pyrite}}$ excursion

reflects only sedimentary environmental perturbation or whether late-diagenetic hydrothermal overprinting also had a role to play.

5.2. Pyrite formation in the Xialei Mn deposit

5.2.1. Timing of formation from petrographic and mineral relationships

The process of sediment-hosted Mn enrichment provides a first-order constraint on the timing of pyrite formation. It begins with the sourcing of dissolved Mn(II) from low temperature hydrothermal systems and the precipitation of Mn(IV)-oxides from the water column at the redoxcline during the sedimentary stage. Early diagenetic reactions in the sediment pile subsequently couple the oxidation of organic matter to the reduction of primary Mn(IV)-oxides and the precipitation of authigenic Mn(II)-carbonates (e.g., Johnson et al., 2016; Maynard, 2010). Crucially, the large volume of Mn in such sediments provides a more suitable terminal electron acceptor than dissolved sulfate (Konhauser et al., 2007) and keeps the Eh at values too high for sulfate reduction (Liu et al., 2006; Maynard, 2010). Hence, in the Xialei Mn deposit, pyrite formation should have postdated the conversion of all Mn(IV)-oxide to Mn(II)-carbonate, which means that pyrite should have formed during early diagenesis or at a later stage. Petrographic investigations corroborate this model (Figs. 3a–d, 4–6): while there is one type of pyrite in the host rocks (Fig. 3a–d) and three different types in the Mn ores (Figs. 4–6), all are present as large-grained, subhedral-euhedral grains, the typical products of diagenesis or later stage processes.

Further detail can be gleaned from petrographic relationships between magnetite and the different pyrite types. The mutually replaceable relationship between Type I pyrite and grainy magnetite (Fig. 4e, g–i) indicates that the formation of magnetite and Type I pyrite was contemporaneous. In our samples, magnetite grains contain abundant Mn(II)-carbonate as inclusions (e.g., Figs. 3f, 4k), which indicate that the magnetite postdates Mn(II)-carbonate formation. The same can be inferred based on magnetite textures and EMPA data showing low concentrations of Ti, V, Ca, and Al, all of it similar to magnetite in banded iron formations (Table 1; Dupuis and Beaudoin, 2011), which are generally considered to have formed through the diagenetic transformation of ferric oxide/hydroxide (Konhauser et al., 2017). The mutually replaceable petrography implies that Type I pyrite must have similarly formed in the diagenetic environment.

A likely origin for Type II and III pyrites then follows based on textural relationships. Type II formed later than Type I as indicated by a consistent petrographic relationship between the two phases, where Type II is present as an overgrowth (Fig. 4a–d, f–g). Type III pyrite appears to stem from the reduction of magnetite, as some pyrite grains are present as magnetite pseudomorphs (Fig. 4k, 5a–d), which have inherited the crystal habit of magnetite and are surrounded by lacy magnetite (Fig. 4j, l, 5e–h). Accordingly, Type III pyrite formed later than magnetite and, by extension, Type I pyrite. Likewise, the subhedral Type III

pyrites in XL-32 contain carbonate as inclusions (Fig. 6a–c) and thus seem to represent the products of diagenesis or late stage alteration. Unfortunately, no direct petrographic comparison can be used to distinguish the relative ages between Type II and Type III pyrites. However, based on the observation that magnetite and recrystallized Mn(II)-carbonate bands occur along the rims of both types of pyrites (Fig. 4c, f, j–l, 6b, j), and more importantly, the consistency in $\delta^{34}\text{S}_{\text{pyrite}}$ between these two types within individual samples (Fig. 7), we suggest that Type II and Type III pyrites are contemporaneous. Further, pyrites in the host rock samples XL-12 and -15 have similar $\delta^{34}\text{S}$ values to Type II and III pyrites in the Mn ores (Fig. 7), and are similarly surrounded by recrystallized carbonate bands (Fig. 3a and b) or magnetite (Fig. 3d), suggesting that these pyrites are the same generation.

5.2.2. Genesis of Type I pyrites

Our *in-situ* sulfur isotope analysis on pyrite in the Xialei Mn deposit reveals positive $\delta^{34}\text{S}_{\text{pyrite}}$ values in the host rock and distinct isotopic signatures between the two pyrite generations in the Mn ores (Fig. 7), i.e., negative $\delta^{34}\text{S}_{\text{pyrite}}$ values for the first generation pyrite (Type I, i.e., inclusion-rich) and highly variable and overall positive $\delta^{34}\text{S}_{\text{pyrite}}$ values for the second generation (Type II and III, i.e., overgrowth and inclusion-poor). Critically, this is a very different picture from the uniformly high positive $\delta^{34}\text{S}_{\text{pyrite}}$ values observed from previous bulk-rock analyses (Qin et al., 2010; Zeng and Liu, 1999). Several factors could affect the sulfur isotopic composition of sulfide minerals, including pH and oxygen fugacity (f_{O_2}) of the fluid, as well as the $\delta^{34}\text{S}$ value of the H_2S that sulfide minerals precipitate from (e.g., Ferrini et al., 2010; Jørgensen et al., 1992; Ohmoto, 1972, 1992). Since, within the stability field of pyrite, not even significant changes in pH and f_{O_2} would produce the large range in $\delta^{34}\text{S}_{\text{pyrite}}$ values observed in the Xialei Mn deposit (Ohmoto, 1972), the variability in the $\delta^{34}\text{S}$ values likely stems from changes in the $\delta^{34}\text{S}$ value of the solution from which the sulfide minerals precipitated. The three common H_2S sources include: (1) seawater sulfate either in the water column or sediment porewaters that is microbially reduced (MSR), with $\delta^{34}\text{S}_{\text{H}_2\text{S}} \approx -50$ to $+20\text{‰}$ (Canfield, 2001a,b, 2004; Goodfellow and Peter, 1996; Ohmoto, 1972, 1992; Ohmoto and Goldhaber, 1997; Ohmoto and Rye, 1979; Shanks et al., 1995); (2) H_2S leached from igneous footwall rocks and/or direct contributions from magmatic fluids with $\delta^{34}\text{S}_{\text{H}_2\text{S}} \approx -5$ to $+5\text{‰}$ (averaging 0‰ ; Marini et al., 2011); and (3) thermochemically reduced preexisting sulfate minerals or seawater sulfate with an initial $\delta^{34}\text{S}_{\text{sulfate}} \approx +4$ to $+33\text{‰}$ (Claypool et al., 1980; Kampschulte and Strauss, 2004; Paytan and Gray, 2012).

Amongst these three possibilities, H_2S leached directly from igneous rocks or fluids are unlikely, as the $\delta^{34}\text{S}$ values of all our studied pyrites are inconsistent with typical near-zero $\delta^{34}\text{S}_{\text{sulfide}}$ values of magmatic sulfur reservoirs (Marini et al., 2011). MSR, on the other hand, is consistent with the negative $\delta^{34}\text{S}$ values in Type I pyrites, ranging from -7.8‰ to -2.0‰ (Fig. 7), even though these values are more positive than the typical MSR products in open-system pore-

waters ($\sim -25\text{‰}$; Bradley et al., 2016; Canfield, 2004; Ohmoto and Goldhaber, 1997). In addition, some of the samples studied here display pyrite grains with gradually increasing $\delta^{34}\text{S}_{\text{pyrite}}$ values along growth from the core towards the edge (e.g., Fig. 4i). Both the modestly negative $\delta^{34}\text{S}$ values and the core-to-rim trend can be attributed to progressively more closed porewater systems leading to increased $\delta^{34}\text{S}_{\text{sulfate}}$ and decreased $\Delta^{34}\text{S}_{\text{sulfate-sulfide}}$. The result is a continuous increase in the $\delta^{34}\text{S}$ of any newly formed pyrite, as predicted by a Rayleigh-type distillation model (Drake et al., 2017; Ferrini et al., 2010; Fischer et al., 2014; Gomes et al., 2018; Marin-Carbonne et al., 2018; Williford et al., 2011). Relatively closed porewater systems may have been the result of increased sedimentation rates during the sea level lowstand driven by the onset of the contemporaneous Gondwana glaciation (Isaacson et al., 2008). Hence, MSR in evolving, closed-system porewaters is a parsimonious explanation for Type I pyrites.

5.2.3. Genesis of second-generation pyrites

5.2.3.1. Microbial sulfate reduction? In contrast to Type I pyrite, the second generation of pyrites (Types II and III) in the Xialei Mn ores, as well as pyrites in the host rock, are characterized by highly positive $\delta^{34}\text{S}_{\text{pyrite}}$ values, some higher than that of contemporaneous sulfate (Fig. 7). While late-stage sulfate-limited MSR in highly closed-system porewaters may explain the increasing $\delta^{34}\text{S}_{\text{pyrite}}$ values of the second-generation pyrites, several lines of evidence suggest otherwise. Firstly, the relationship of mineral textures (see Section 5.2.1) is more compatible with two separate mineralizing events for Type I and Type II pyrites (e.g., Fig. 4a–d). Secondly, the large span of sulfur isotope data between Type I and Type II pyrites, as well as the small intra-crystalline variation of $\delta^{34}\text{S}$ values in some Type III pyrites (Fig. 6a–b, o) and host-rock pyrites (Fig. 3a–b), does not conform to the continuously increasing micrometer-scale $\delta^{34}\text{S}$ pattern related to Rayleigh fractionation during MSR in a closed system. Thirdly, the decreasing $\delta^{34}\text{S}$ trend from the core to the edge in some other Type III pyrite grains (Fig. 6d–f) is opposite to that expected of MSR. Finally, although Type III and host-rock pyrites with $\delta^{34}\text{S}_{\text{pyrite}}$ values exceeding $\delta^{34}\text{S}_{\text{sulfate}}$ (Fig. 3c–d, 6j) can be explained through oxidative reworking of ambient H_2S (see Section 5.1), the conservation of Mn(II)-carbonate requires anoxic conditions, precluding such oxidative processes in these sediments. All together, previous models based on MSR and pyrite re-oxidation are a poor fit for the positive- $\delta^{34}\text{S}$ pyrites in the Xialei Mn deposit.

5.2.3.2. Thermochemical sulfate reduction. Accordingly, we propose that the positive $\delta^{34}\text{S}$ pyrites in the Xialei Mn deposit formed instead by TSR in sulfate-bearing hydrothermal fluids. This interpretation is supported by multiple lines of sedimentological and geochemical evidence as listed below:

- (i) Temperature data: The Xialei manganese deposit hosts Mn-silicate minerals, including tephroite and spessartine, with rhodonites cross-cutting the earlier Mn(II)-carbonate laminations (Zeng and Liu,

1999). These minerals were formed through late-stage alteration and silicification of early diagenetic Mn-carbonate during deeper burial diagenesis or metamorphism (e.g., Johnson et al., 2016; Zeng and Liu, 1999). The formation of tephroite and spessartine requires relatively high temperatures of ~250–300 °C, whereas the formation temperature of rhodonite exceeds 250 °C (Brusnitsyn, 2006; Brusnitsyn et al., 2017). The occurrence of these high-temperature minerals clearly indicates that the Xialei Mn deposit experienced a later hydrothermal event.

- (ii) Tectonic activity: The Xialei Mn metallogenic episode was a response to the initial opening stage of the Palaeo-Tethys Ocean along the Gondwana margin (Chen et al., 2018; Deng and Wang, 2016), which could have enhanced the development of faults and hydrothermal activity. This is exemplified by the late stage, high temperature rhodonite veins (Zeng and Liu, 1999) that vertically crosscut the thin, wavy Mn-carbonate laminae, reflecting the upward migration of secondary hydrothermal fluids. Intrusion of an external sulfate-rich hydrothermal fluid could facilitate the mineralization of these positive $\delta^{34}\text{S}$ pyrites via TSR.
- (iii) Pyrite petrography: In contrast with MSR that dominantly occurs in the water column or early-diagenesis porewater (Bowles et al., 2014; Jørgensen and Kasten, 2006), TSR usually takes place relatively late during deep burial diagenesis. The positive- $\delta^{34}\text{S}$ pyrites post-dated the MSR-derived Type I pyrite (see discussion in Section 5.2.1), which is consistent with this sequence. In addition, both Type III and host-rock pyrites are dominantly euhedral in shape. These features are similar to those of the Dajiangping SEDEX-Type pyrites from the Youjiang Basin in South China, deposited during the Late Devonian, that have been demonstrated to be of hydrothermal origin (Qiu et al., 2018). Similar clean overgrowth textures as seen in our Type II pyrites have also been reported from ancient volcanogenic massive sulfide (VMS) deposits (e.g., Brueckner et al., 2014; Ulrich et al., 2011; Wagner et al., 2004), which are considered to have formed through TSR. Finally, recrystallized (Mn-)carbonate aligned along the edges of Type II, Type III, and host rock pyrites (Figs. 3a–b, 4c, j–l, 6b, j) has also been proposed to form during deeper burial processes together with Mn-silicates (Johnson et al., 2016).
- (iv) Sulfur isotopes: The sulfur isotope signatures of the Type II, Type III, and host-rock pyrites (and that of the paragenetic ZnS; Fig. 6i) are distinct from that of Type I pyrites (Fig. 7). In the host rock, $\delta^{34}\text{S}_{\text{pyrite}}$ is homogeneous within grains, with some values higher than those of contemporaneous seawater (e.g., sample XL-15; Fig. 3c–d). In the Mn ores, our high-resolution analyses indicate that most Type II and Type III pyrite grains have relatively homogeneous intra-grain isotopic compositions around +13‰ (e.g., Figs. 4c–d, 6a–b). Others show more positive values up to +18‰ (Fig. 6h–i) or even exceed the

$\delta^{34}\text{S}$ value of contemporaneous seawater sulfate (Fig. 6j). In addition, some Type III pyrite grains show variable intra-grain isotopic compositions with $\delta^{34}\text{S}_{\text{pyrite}}$ values decreasing from core to edge (Fig. 6d–f). Lab experiments on the kinetic isotopic fractionation during TSR have demonstrated that as temperature decreases, $\Delta^{34}\text{S}_{\text{sulfate-sulfide}}$ increases, leading to a decrease in $\delta^{34}\text{S}_{\text{pyrite}}$ (e.g., Kiyosu, 1980; Kiyosu and Krouse, 1990; Ohmoto and Goldhaber, 1997). Accordingly, a gradient of decreasing $\delta^{34}\text{S}_{\text{pyrite}}$ values would be expected for individual pyrite grains developed during TSR as hydrothermal fluids progressively cooled (Cui et al., 2018; Kiyosu and Krouse, 1990) – the observed isotopic patterns of these positive- $\delta^{34}\text{S}$ pyrites can be satisfactorily explained by TSR.

5.2.4. Influence of metamorphism on sulfur isotope composition?

Considering the presence of Mn(II)-silicate minerals, and their probable origin as the product of contact metamorphism (e.g., Zeng and Liu, 1999), it is necessary to test whether closed-system (i.e., without involvement of external sulfate) recrystallization of Type I pyrites could explain the sulfur isotope features observed in Type II and III pyrites from the Mn ores. The effects of metamorphic recrystallization on sulfur isotope composition have been extensively discussed, particularly regarding their fractionation in VMS sulfides (Seal, 2006). However, Brueckner et al. (2014), Cook and Hoefs (1997), Seccombe et al. (1985), Ulrich et al. (2011) and Wagner et al. (2004) all suggested that sulfur isotope equilibration caused by metamorphism is locally restricted and most sulfur isotope data can still represent original $\delta^{34}\text{S}$ compositions. Furthermore, Wagner and Boyce (2006) studied two types of pyrites: syn-depositional pyrite and pyrite overgrowths in the Devonian Hunsrück Slate from Germany, and suggested that metamorphic recrystallization did not result in a significant modification of the primary sulfur isotopic composition of these phases. Based solely on the petrographic features of the samples studied here, the Type II and III pyrites may have been produced by the recrystallization of Type I pyrites; however, given the likelihood of the original $\delta^{34}\text{S}$ to be preserved, the very different sulfur isotope values of these pyrite generations suggest against such a recrystallization pathway.

5.3. Sulfur source for the high $\delta^{34}\text{S}$ pyrites in the Xialei Mn deposits

The positive $\delta^{34}\text{S}$ values of the secondary pyrites require sulfate-rich hydrothermal fluids which could be derived from the dissolution of preexisting sulfate minerals. Potential sulfate sources for the Xialei Mn deposit are the well-known Devonian stratiform barites and vein-hosting Pb-Zn barites in the Youjiang Basin. The former is hosted in the Liujiang Formation chert beds of Late Devonian age and the latter are concentrated in the underlying Early to Middle Devonian sediments (Chen and Gao, 1988). The

sulfur isotope ratios of most of the stratiform barites are concentrated around +30‰, despite a few higher values (34.7‰, 37.5‰, and 41.9‰) also occurring. The sulfur isotope composition of the underlying vein-hosting Pb-Zn barite ranges from +20‰ to +31‰ (averaging +25‰), and corresponds better to that of the Late Devonian seawater (~23‰; [Chen and Gao, 1988](#); [Li, 2007](#)). Based on the similar chemical compositions and homogenization temperatures obtained from fluid inclusions, [Chen and Gao \(1988\)](#) and [Li \(2007\)](#) suggested that the sulfate in the stratiform and vein-hosted Pb-Zn barites may have both originated from Late Devonian seawater. The slight ³⁴S-enrichment of the stratiform barites compared to seawater values could be due to the high and episodic sedimentation rate in a local depositional setting, resulting in closed-system isotope behavior. We propose that dissolution of this barite could have been the source of hydrothermal sulfate for the TSR in the Xialei Mn deposit, which formed the Type II and III, and host-rock pyrites.

5.4. TSR model for isotopically positive pyrite formation

To generate pyrites with a $\delta^{34}\text{S}$ value up to +37.6‰, as observed in sample XL-63, the $\delta^{34}\text{S}$ values of their parent sulfate in the hydrothermal fluid needed to be at least +38‰. To assess whether this is achievable, we modeled the extent of TSR required to reach a $\delta^{34}\text{S}_{\text{sulfate}}$ value of 38‰ from an initial value of 30‰ (i.e., the average of the barite beds) and at a temperature range of 250–300 °C (based on the discussion in Section 5.3.2.2) in [Fig. 8](#).

If the TSR occurred in an open system (the Rayleigh model), where the sulfide product was immediately removed and could not follow the hydrothermal fluid to the site of sample XL-63, then according to [Li et al. \(2016\)](#), the required extent of TSR can be calculated by the equation below:

$$f = e^{\frac{1}{\alpha} \ln \left(\frac{\delta_f + 1}{\delta_0 + 1} \right) - \ln \left[\frac{1 + (\delta_0 + 1) R_{\text{VCDT}}}{1 + (\delta_f + 1) R_{\text{VCDT}}} \right]} \quad (1)$$

where f refers to the fraction of remaining sulfate relative to the initial sulfate; ϵ refers to a kinetic isotope enrichment factor in ‰ between the product sulfide and substrate sulfate,

$$\epsilon = 4.19 - 3.32 * 10^6 / T^2 \quad (2)$$

(T refers to temperature in Celsius) which is $-48.9‰$ at 250 °C and $-32.7‰$ at 300 °C based on the experimental constraints by [Kiyosu and Krouse \(1990\)](#); δ_0 and δ_f refer to the $\delta^{34}\text{S}$ values of the initial and remaining sulfate, respectively; R_{VCDT} is the $^{34}\text{S}/^{32}\text{S}$ of the Vienna Cañon Diablo Troilite (VCDT) standard and equals to 0.04416 ([Ding et al., 2001](#)). Inputting 30‰ for δ_0 and 38‰ for δ_f to Eq. (1), the yielded f value is 85% at 250 °C and 79% at 300 °C ([Fig. 8](#)). This suggests at least 15–21% sulfate would have been pre-reduced before the TSR formation of pyrite in sample XL-63.

If TSR occurred as a closed system (the batch model), the extent of TSR can be calculated by the equation below ([Li et al., 2016](#)):

$$f = \frac{\delta_0 + 1 - \alpha \cdot (1 + \delta_f)}{(1 - \alpha) \cdot (1 + \delta_f)} e \quad (3)$$

where α refers to the equilibrium isotope fractionation factor between sulfide and sulfate, and the other symbols are the same as those in Eq. (1). At an α value of 0.9751 at 250 °C ([Shanks et al., 1981](#)) and 0.9802 at 300 °C ([Sakai and Dickson, 1978](#)), the f value is 0.69 for 250 °C and 0.61 for 300 °C, respectively ([Fig. 8](#)). This requires 31–39% sulfate to be pre-reduced before the TSR formation of pyrite in sample XL-63. In summary, the conditions required for the formation of high $\delta^{34}\text{S}_{\text{sulfate}}$ values (>+38‰) in either an open or closed system during the upward migration of hydrothermal fluids along faults are not difficult to achieve.

Following the infiltration of these hydrothermal fluids into the studied strata, pyrites with varying positive $\delta^{34}\text{S}$ values may have formed via TSR at different $\Delta^{34}\text{S}_{\text{sulfate-sulfide}}$ values. The cooling of the hydrothermal flu-

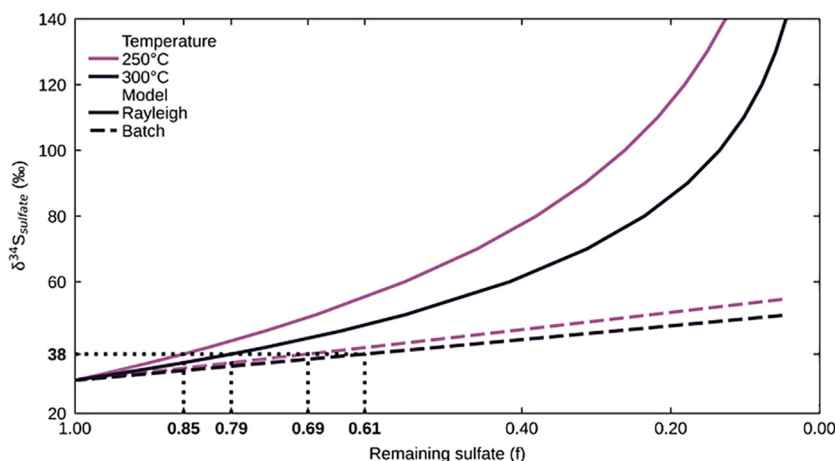


Fig. 8. Models of $\delta^{34}\text{S}_{\text{sulfate}}$ evolution during the precipitation of pyrite under open system Rayleigh distillation (solid line) and closed system batch equilibration (dashed line) conditions at 250 °C (light purple) and 300 °C (dark purple). The initial $\delta^{34}\text{S}_{\text{sulfate}}$ was set at 30‰. Equations used in the calculation are from [Li et al. \(2016\)](#). Black arrows indicate the points at which $\delta^{34}\text{S}_{\text{sulfate}}$ reaches +38‰. See the main text for detailed discussion. (For interpretation of the references to colour in this figure legend, the reader is referred to the web version of this article.)

ids appears to be responsible for the negative $\delta^{34}\text{S}_{\text{pyrite}}$ shifts at microscopic scales, i.e., the negative shifts within individual Type III pyrite grains, as discussed in Section 5.2.3.2.

5.5. Predominantly ^{34}S -enriched pyrites in Mn ores

It is interesting to note that, despite Mn mineralization having supposedly little effect on the fundamentals of pyrite precipitation, many sediment-hosted Mn ores display characteristically positive $\delta^{34}\text{S}_{\text{pyrite}}$ values (Fig. 9). This hints at a common mechanism affecting pyrite formation in such deposits, but there is no consensus yet as to whether this is tied to microbial or abiotic processes. Pyrites with positive $\delta^{34}\text{S}$ values formed via MSR may show a

transient decrease in $\Delta^{34}\text{S}_{\text{sulfate-sulfide}}$, either because of low sulfate concentrations in the regional water column (Li et al., 2012; Liu et al., 2006) and/or enhanced closed-system behavior in the porewater, which could be aided by a decrease in porewater porosity through Mn(II)-carbonate precipitation (Okita and Shanks, 1992) and high sedimentation rates characteristic of Mn ores (Polgári et al., 2016). However, other studies have proposed that such pyrites may be attributed to TSR coincident to hydrothermal fluid alteration during late burial diagenesis, instead of MSR (Cui et al., 2018; Johnson et al., 2013). Our results of pyrites in Xialei Mn deposit fall into the latter option. On the whole, models of the formation of ^{34}S -enriched pyrites in Mn ores are mostly

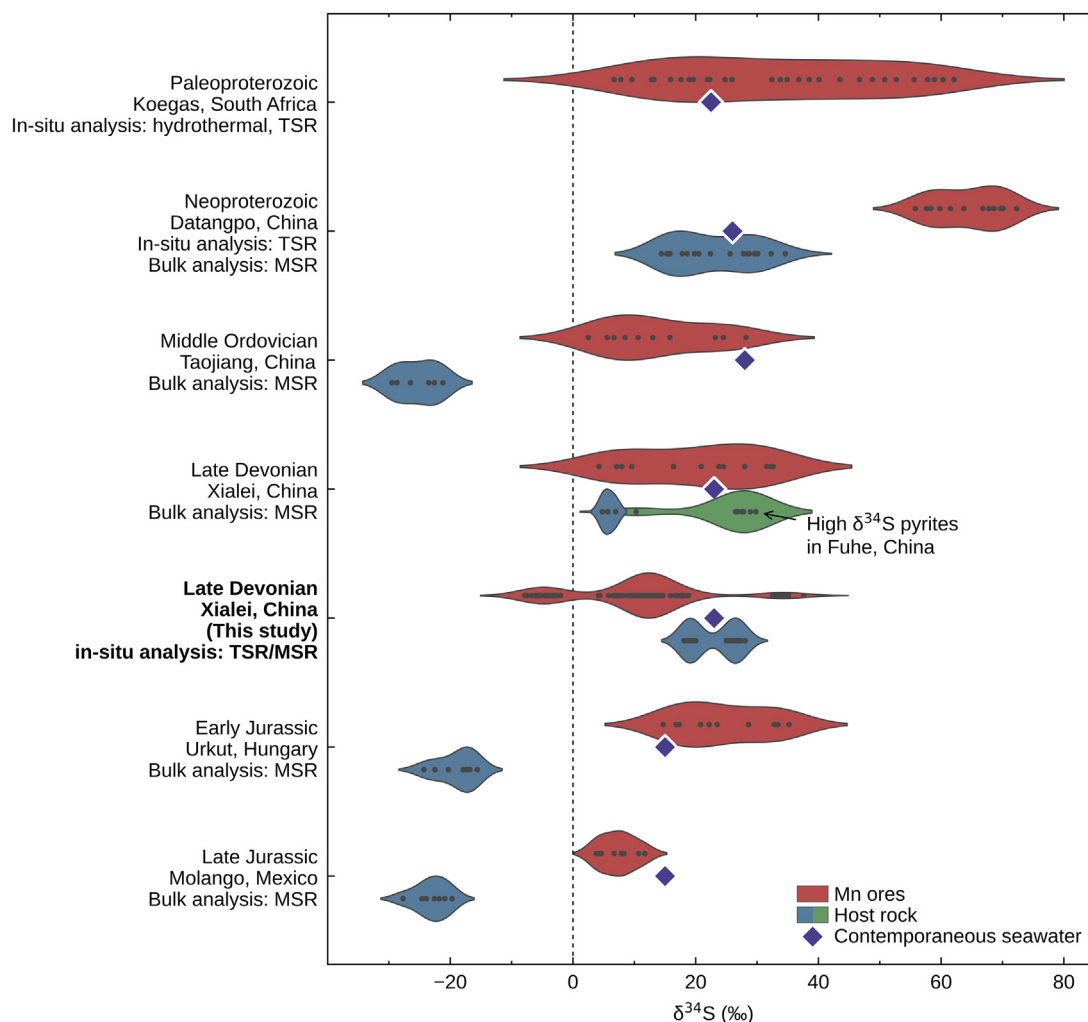


Fig. 9. Compilation of published $\delta^{34}\text{S}_{\text{pyrite}}$ data in different Mn deposits through time with measurements in this study and their corresponding interpretations (left-hand side). Y-axis represents $\delta^{34}\text{S}_{\text{pyrite}}$ values. Black dots within violin plots represent individual data points. Purple diamonds represent contemporaneous seawater $\delta^{34}\text{S}_{\text{sulfate}}$ values for the respective time period (Kampschulte and Strauss, 2004). Some plotted data were generated by conventional bulk-rock $\delta^{34}\text{S}$ analysis, others by in-situ $\delta^{34}\text{S}$ analysis. Note: many $\delta^{34}\text{S}_{\text{pyrite}}$ measurements exceed the contemporaneous $\delta^{34}\text{S}_{\text{sulfate}}$ value. Abbreviations: MSR = microbial sulfate reduction; TSR = thermochemical sulfate reduction. Data are from: Cui et al. (2018), Johnson et al. (2013), Liu et al. (2006), Okita and Shanks (1992), Polgári et al. (2016), Qin et al. (2010), and Zeng and Liu (1999). (For interpretation of the references to colour in this figure legend, the reader is referred to the web version of this article.)

linked with common geological factors that affect pyrite evolution in all marine sedimentary rocks.

6. IMPLICATIONS

Previous work on anomalously positive sulfur isotope values in Late Devonian pyrites has relied on bulk-rock analysis and has attributed the small isotope fractionations to MSR in sulfate limited conditions, leading to speculation regarding changes in the marine redox state and a decline in sulfate concentrations in seawaters or porewaters. In addition, a difference in the magnitude of the sulfur isotope excursion was found between the carbonates and sediment-hosted Mn ores of the Youjiang Basin, South China, and was previously considered to be mainly caused by differences in local sedimentary conditions (Chen et al., 2013; Qin et al., 2010; Zeng and Liu, 1999). However, our new in-situ analyses of the Xialei Mn deposit clearly indicate that at least some Late Devonian pyrites that were previously defined as syndepositional in origin actually consist of at least two distinct generations. Based on our petrographic and isotopic evidence, we argue that the positive $\delta^{34}\text{S}_{\text{pyrite}}$ and reversed $\Delta^{34}\text{S}_{\text{sulfate-sulfide}}$ values recorded in the Xialei Mn deposit represent the result of TSR during late hydrothermal alteration, rather than primary sedimentation. In addition, the formation of the Xialei Mn deposit and neighboring sedimentary strata (limestone) appear to be synchronous with the initial opening of the Palaeo-Tethys Ocean along the Gondwana margin (Chen et al., 2018; Deng and Wang, 2016), which played a key role in facilitating active rifting and hydrothermal activity. Given the stratigraphic relationship between the Xialei Mn deposit and the Fuhe section in the same (Youjiang) basin and the possible existence of a basin-wide hydrothermal system of vertically upward fluid migration along a fault system, we speculate that superheavy $\delta^{34}\text{S}_{\text{pyrite}}$ values in the Fuhe section (Chen et al., 2013) may also have been generated via hydrothermal alteration, and require careful reassessment by high-resolution in-situ analysis in the future.

Recent studies hypothesize that local depositional environments may impact rates of sedimentation and sulfide oxidation. This consequently could lead to $\Delta^{34}\text{S}_{\text{sulfate-sulfide}}$ variations during MSR, which provides a reasonable mechanism for explaining positive $\delta^{34}\text{S}_{\text{pyrite}}$ values through entirely local processes (e.g., Bryant et al., 2019; Fike et al., 2015; Pasquier et al., 2017; Richardson et al., 2019a; Rose et al., 2019). Our results, combined with recent interpretations that some Neoproterozoic “superheavy” pyrites from South China were also generated by TSR (Cui et al., 2018), hint that TSR is a similarly wide-spread process in generating positive $\delta^{34}\text{S}_{\text{pyrite}}$ records, particularly in sections associated with extensive tectonic activity. Previous hypotheses that tie positive $\delta^{34}\text{S}_{\text{pyrite}}$ values with noteworthy global biogeochemical events should be reassessed to account for both of these mechanisms. If such processes are found to be significant, these anomalous isotope values should, therefore, not be used for local and/or global paleoenvironmental reconstructions, since they only reflect local or post-

depositional phenomena. Our study shows how multiple lines of sedimentological and geochemical evidence at both basin and micrometer scales are essential for accurate de-convolution of the numerous geochemical processes contributing to proxy data in the rock record.

7. CONCLUSIONS

Detailed petrographic and in-situ $\delta^{34}\text{S}$ analyses of pyrite found in a Late Devonian Mn deposit in the Youjiang Basin of South China have identified at least two generations of pyrites. The earliest generation is characterized by negative $\delta^{34}\text{S}_{\text{pyrite}}$ values that suggest a biogenic origin through MSR. The later generations, characterized by positive $\delta^{34}\text{S}_{\text{pyrite}}$ values up to 37.6‰, are tied to hydrothermal processes and TSR, not to low water column sulfate concentrations and/or pyrite re-oxidation, as has been previously suggested for “superheavy” pyrites. Hydrothermal fluids carrying ^{34}S -enriched sulfur from the preexisting barite beds in the underlying Frasnian strata potentially also altered the correlative strata of the Fuhe region in which highly positive $\delta^{34}\text{S}_{\text{pyrite}}$ values were previously linked to the evolution of the local sulfur cycle. We propose that post-depositional TSR, associated with hydrothermal activities induced by tectonic rifting during the opening of the Palaeo-Tethyan Ocean, played an important role in generating positive $\delta^{34}\text{S}_{\text{pyrite}}$ values, at least in South China. Accordingly, leveraging advancements in in-situ microanalysis, reassessments of previously reported transient increases in $\delta^{34}\text{S}_{\text{pyrite}}$ that have traditionally been associated with noteworthy biogeochemical events in the Earth’s history are needed to fully assess the potential effect of TSR in other strata, particularly those located in tectonically active regions.

Declaration of Competing Interest

The authors declare that they have no known competing financial interests or personal relationships that could have appeared to influence the work reported in this paper.

ACKNOWLEDGEMENTS

We thank Dr. Kui-Dong Zhao and Shui-Yuan Yang for their assistance with in situ sulfur isotope and mineral chemistry measurements, and three anonymous reviewers for improving the interpretations and the manuscript. This work was financially supported by the National Natural Science Foundation of China (41972091) to DHP, the Fundamental Research Funds for the Central Universities, China University of Geosciences in Wuhan (CUGCJ1711) and the special fund from the State Key Laboratory of Geological Processes and Mineral Resources, China University of Geosciences (no. MSFGPMR03-2) to SYJ, and support from the Packard Foundation to NJP.

APPENDIX A. SUPPLEMENTARY MATERIAL

Supplementary data to this article can be found online at <https://doi.org/10.1016/j.gca.2020.05.017>.

REFERENCES

- Algeo T. J., Luo G. M., Song H. Y., Lyons T. W. and Canfield D. E. (2015) Reconstruction of secular variation in seawater sulfate concentrations. *Biogeosciences* **12**, 2131–2151.
- Aller R. C., Madrid V., Chistoserdov A., Aller J. Y. and Heilbrun C. (2010) Unsteady diagenetic processes and sulfur biogeochemistry in tropical deltaic muds: implications for oceanic isotope cycles and the sedimentary record. *Geochim. Cosmochim. Acta* **74**, 4671–4692.
- Berner R. A. (1989) Biogeochemical cycles of carbon and sulfur and their effect on atmospheric oxygen over Phanerozoic time. *Glob. Planet. Chang.* **1**, 97–122.
- Berner R. A. and Raiswell R. (1983) Burial of organic carbon and pyrite sulfur in sediments over Phanerozoic time: a new theory. *Geochim. Cosmochim. Acta* **47**, 855–862.
- BGMRG (Bureau of Geology and Mineral Resources of Guangxi Zhuang Autonomous Region), 1985, Regional geology of Guangxi Zhuang autonomous region: Beijing, Geological Publishing House, p. 853 (in Chinese with English Abstract).
- Böttcher M. E. (2011) Sulfur isotopes. In *Encyclopedia of Geobiology* (eds. J. Reitner and V. Thiel). Springer Netherlands, pp. 864–866.
- Bowles M. W., Mogollón J. M., Kasten S., Zabel M. and Hinrichs K. U. (2014) Global rates of marine sulfate reduction and implications for sub-sea-floor metabolic activities. *Science* **344**, 889–891.
- Bradley A. S., Leavitt W. D., Schmidt M., Knoll A. H., Girguis P. R. and Johnston D. T. (2016) Patterns of sulfur isotope fractionation during microbial sulfate reduction. *Geobiology* **14**, 91–101.
- Brueckner S. M., Piercy S. J., Layne G. D., Piercy G. and Sylvester P. J. (2014) Variations of sulphur isotope signatures in sulphides from the metamorphosed Ming Cu(–Au) volcanogenic massive sulphide deposit, Newfoundland Appalachians, Canada. *Miner. Deposita* **50**, 619–640.
- Brusnitsyn A. I. (2006) Mineralogy and metamorphism conditions of manganese ore at the South Faizulino deposit, the southern Urals, Russia. *Geol. Ore Depos.* **48**, 193–214.
- Brusnitsyn A. I., Starikova E. V. and Zhukov I. G. (2017) Mineralogy of low grade metamorphosed manganese sediments of the Urals: Petrological and geological applications. *Ore Geol. Rev.* **85**, 140–152.
- Bryant R. N., Jones C., Raven M. R., Gomes M. L., Berelson W. M., Bradley A. S. and Fike D. A. (2019) Sulfur isotope analysis of microcrystalline iron sulfides using secondary ion mass spectrometry imaging: Extracting local paleo-environmental information from modern and ancient sediments. *Rapid Commun. Mass Spectrom.* **33**, 491–502.
- Canfield D. E. (2001a) Biogeochemistry of sulfur isotopes. Stable Isotope Geochemistry (eds. J. W. Valley and D. Cole). Mineralogical Society of America and Geochemical Society. *Rev. Mineral. Geochem.* **43**, 607–636.
- Canfield D. E. (2001b) Isotope fractionation by natural populations of sulfate-reducing bacteria. *Geochim. Cosmochim. Acta* **65**, 1117–1124.
- Canfield D. E. (2004) The evolution of the Earth surface sulfur reservoir. *Am. J. Sci.* **304**(10), 839–861.
- Canfield D. E. and Farquhar J. (2012) The global sulfur cycle. In *Fundamentals of Geobiology* (eds. A. H. Knoll, D. E. Canfield and K. O. Konhauser). Wiley, pp. 49–64.
- Canfield D. E. and Teske A. (1996) Late Proterozoic rise in atmospheric oxygen concentration inferred from phylogenetic and sulphur-isotope studies. *Nature* **382**, 127–132.
- Canfield D. E., Farquhar J. and Zerkle A. L. (2010) High isotope fractionations during sulfate reduction in a low-sulfate euxinic ocean analog. *Geology* **38**, 415–418.
- Chen C. L. and Shi X. Y. (2006) Sedimentary and tectonic evolution of Late Paleozoic deep-water strata in the Youjiang basin. *Geol. China* **33**, 436–443 (in Chinese with English abstract).
- Chen D. Z., Wang J. G., Racki G., Li H., Wang C. Y., Ma X. P. and Whalen M. T. (2013) Large sulfur isotopic perturbations and oceanic changes during the Frasnian-Famennian transition of the Late Devonian. *J. Geol. Soc. Lond.* **170**, 465–476.
- Chen F. G., Wang Q. F., Yang S. J., Zhang Q. Z., Liu X. F., Chen J. H. and Carranza E. J. M. (2018) Spacetime distribution of manganese ore deposits along the southern margin of the South China Block, in the context of Palaeo-Tethyan evolution. *Int. Geol. Rev.* **60**(1), 72–86.
- Chen H. M., Wu X. H., Zhang Y., Li Y. X. and Wen Q. Y. (1994) Carboniferous lithofacies paleogeography and mineralization in South China. Geological Publishing House, Beijing, pp. 69–73 (in Chinese with English abstract).
- Chen X. P. and Gao J. Y. (1988) Thermal water deposition and Pb-Zn Barite deposits in the Devonian system, central Guangxi. *Chin. J. Geochem.* **7**, 321–328.
- Claypool G. E., Holser W. T., Kaplan I. R., Sakai H. and Zak I. (1980) The age curves of sulfur and oxygen 498 isotopes in marine sulfate and their mutual interpretation. *Chem. Geol.* **28**, 199–260.
- Cong Y., Dong Q. J., Xiao K. Y., Chen J. P., Gao Y. B. and Yin J. N. (2018) Characteristics and predicted potential of Mn resources in China. *Earth Sci. Front.* **25**(3), 118–137 (in Chinese with English abstract).
- Cook N. J. and Hoefs J. (1997) Sulphur isotope characteristics of metamorphosed Cu-(Zn) volcanogenic massive sulphide deposits in the Norwegian Caledonides. *Chem. Geol.* **135**, 307–324.
- Crowe S. A., Paris G., Katsev S., Jones C., Kim S. T., Zerkle A. L., Nomosatryo S., Fowle D. A., Adkins J. F. and Sessions A. L. (2014) Sulfate was a trace constituent of Archean seawater. *Science* **346**, 735–739.
- Cui H., Kitajima K., Spicuzza M. J., Fournelle J. H., Denny A., Ishida A., Zhang F. F. and Valley J. W. (2018) Questioning the biogenicity of Neoproterozoic superheavy pyrite by SIMS. *Am. Mineral.* **103**(9), 1362–1400.
- Deng J. and Wang Q. F. (2016) Gold mineralization in China: Metallogenic provinces, deposit types and tectonic framework. *Gondwana Res.* **36**, 219–274.
- Ding T., Valkiers S., Kipphardt H., Bievre P. D., Taylor P. D. P., Gonfiantini R. and Krouse R. (2001) Calibrated sulfur isotope abundance ratios of three IAEA sulfur isotope reference materials and V-CDT with a reassessment of the atomic weight of sulfur. *Geochim. Cosmochim. Acta* **65**, 2433–2437.
- Drake H., Heim C., Roberts N. M. W., Zack T., Tillberg M., Broman C., Ivarsson M., Whitehouse M. J. and Åström M. E. (2017) Isotopic evidence for microbial production and consumption of methane in the upper continental crust throughout the Phanerozoic eon. *Earth Planet. Sci. Lett.* **470**, 108–118.
- Du Y. S., Huang H., Yang J. H., Huang H. W., Tao P., Huang Z. Q., Hu L. S. and Xie C. X. (2013) The basin translation from late Paleozoic to Triassic of the Youjiang basin and its tectonic signification. *Geol. Rev.* **59**, 1–10 (in Chinese with English abstract).
- Dupuis C. and Beaudoin G. (2011) Discriminant diagrams for iron oxide trace element fingerprinting of mineral deposit types. *Mineral. Deposita* **46**(4), 319–335.

- Eldridge D. L., Guo W. and Farquhar J. (2016) Theoretical estimates of equilibrium sulfur isotope effects in aqueous sulfur systems: highlighting the role of isomers in the sulfite and sulfoxylate systems. *Geochem. Cosmochim. Acta* **195**, 171–200.
- Ferrini V., Fayek M., DeVito C., Mignardi S. and Pignatti J. (2010) Extreme sulfur isotope fractionation in the deep Cretaceous biosphere. *J. Geol. Soc.* **167**, 1009–1018.
- Fike D. A. and Grotzinger J. P. (2008) A paired sulfate–pyrite $\delta^{34}\text{S}$ approach to understanding the evolution of the Ediacaran–Cambrian sulfur cycle. *Geochim. Cosmochim. Acta* **72**, 2636–2648.
- Fike D. A., Bradley A. S. and Rose C. V. (2015) Rethinking the ancient sulfur cycle. *Ann. Rev. Earth Planet. Sci.* **43**, 593–622.
- Fike D. A., Grotzinger J. P., Pratt L. M. and Summons R. E. (2006) Oxidation of the Ediacaran ocean. *Nature* **444**, 744–747.
- Fischer W. W., Fike D. A., Johnson J. E., Raub T. D., Guan Y., Kirschvink J. L. and Eiler J. M. (2014) SQUID–SIMS is a useful approach to uncover primary signals in the Archean sulfur cycle. *Proc. Natl. Acad. Sci.* **111**, 5468–5473.
- Friedman I. and O’Neil J. R. (1977) Data of geochemistry: Compilation of stable isotope fractionation factors of geochemical interest. *Geol. Surv. Prof. Pap.* **440**, KK1–KK12 (Chapter KK).
- Fry B., Ruf W., Gest H. and Hayes J. M. (1988) Sulfur isotope effects associated with oxidation of sulfide by O_2 in aqueous solution. *Chem. Geol.* **73**(3), 205–210.
- Gao J., Fike D. A. and Aller R. C. (2013) Enriched pyrite $\delta^{34}\text{S}$ signals in modern tropical deltaic muds. *AGU 2013 Annual Meeting, San Francisco, CA*, p. B31A-0352.
- Garrels R. M. and Lerman A. (1981) Phanerozoic cycles of sedimentary carbon and sulfur. *Proc. Natl. Acad. Sci.* **78**, 4652–4656.
- Geldsetzer H. H. J., Goodfellow W. D., McLaren D. J. and Orchard J. (1987) Sulphur isotope anomaly associated with the Frasnian–Famennian extinction, Medicine Lake, Alberta, Canada. *Geology* **15**, 393–396.
- Gill B. C., Lyons T. W. and Saltzman M. R. (2007) Parallel, high-resolution carbon and sulfur isotope records of the evolving Paleozoic marine sulfur reservoir. *Palaeogeogr. Palaeoclimatol. Palaeoecol.* **256**, 156–173.
- Goldstein T. P. and Aizenshtat Z. (1994) Thermochemical sulfate reduction: A review. *J. Therm. Anal.* **42**, 241–290.
- Gomes M. L., Fike D. A., Bergman K. D. and Knoll A. H. (2018) Environmental insights from high-resolution (SIMS) sulfur isotope analyses of sulfides in Proterozoic microbialites with diverse mat textures. *Geobiology* **16**, 17–34.
- Gomes M. L. and Hurtgen M. T. (2015) Sulfur isotope fractionation in modern euxinic systems: Implications for paleoenvironmental reconstructions of paired sulfate–sulfide isotope records. *Geochim. Cosmochim. Acta* **157**, 39–55.
- Goodfellow W. D. and Peter J. M. (1996) Sulphur isotope composition of the Brunswick no. 12 massive sulphide deposit, Bathurst Mining Camp, New Brunswick: implications for ambient environment, sulphur source, and ore genesis. *Can. J. Earth Sci.* **33**(2), 231–251.
- Habicht K. S. and Canfield D. E. (2001) Isotope fractionation by sulfate reducing natural populations and the isotopic composition of sulfide in marine sediments. *Geology* **29**, 555–558.
- Habicht K. S., Gade M., Thamdrup B., Berg P. and Canfield D. E. (2002) Calibration of sulfate levels in the Archean ocean. *Science* **298**, 2372–2374.
- Hints O., Martma T., Männik P., Nõlvak J., Põldvere A., Shen Y. and Viira V. (2014) New data on Ordovician stable isotope record and conodont biostratigraphy from the Viki reference drill core, Saaremaa Island, western Estonia. *GFF* **136**, 100–104.
- Holland H. D. (1973) Systematics of isotopic composition of sulfur in oceans during the Phanerozoic and its implications for atmospheric oxygen. *Geochim. Cosmochim. Acta* **37**, 2605–2616.
- Horita J., Zimmermann H. and Holland H. D. (2002) Chemical evolution of seawater during the Phanerozoic: implications from the record of marine evaporites. *Geochem. Cosmochim. Acta* **66**, 3733–3756.
- Huang C., Song J. J., Shen J. and Gong Y. M. (2018) The influence of the Late Devonian Kellwasser events on deep-water ecosystems: Evidence from palaeontological and geochemical records from South China. *Palaeogeogr. Palaeoclimatol. Palaeoecol.* **504**, 60–74.
- Hurtgen M. T., Pruss S. B. and Knoll A. H. (2009) Evaluating the relationship between the carbon and sulfur cycles in the later Cambrian ocean: an example from the Port au Port Group, western Newfoundland, Canada. *Earth Planet. Sci. Lett.* **281**, 288–297.
- Isaacson P. E., Díaz-Martínez E., Grader G. W., Kalvoda J., Babek O. and Devuyst F. X. (2008) Late-Devonian–earliest Mississippian glaciation in Gondwanaland and its biogeographic consequences. *Palaeogeogr. Palaeoclimatol. Palaeoecol.* **268**, 126–142.
- Jiang L., Worden R. H. and Cai C. (2015) Generation of isotopically and compositionally distinct water during thermochemical sulfate reduction (TSR) in carbonate reservoirs: Triassic Feixianguan Formation, Sichuan Basin, China. *Geochim. Cosmochim. Acta* **165**, 249–262.
- Jiang L., Worden R. H. and Yang C. (2018) Thermochemical sulphate reduction can improve carbonate petroleum reservoir quality. *Geochim. Cosmochim. Acta* **223**, 127–140.
- Joachimski M. M., Ostertag-Henning C., Pancost R. D., Strauss H., Freeman K. H., Littke R., Sinningh-Damste J. S. and Racki G. (2001) Water column anoxia, enhanced productivity and concomitant changes in $\delta^{13}\text{C}$ and $\delta^{34}\text{S}$ across the Frasnian–Famennian boundary (Kowala–Holy Cross Mountains/Poland). *Chem. Geol.* **175**, 109–131.
- Johnston D. T., Wing B. A., Farquhar J., Kaufman A. J., Strauss H., Lyons T. W., Kah L. C. and Canfield D. E. (2005) Active microbial sulfur disproportionation in the Mesoproterozoic. *Science* **310**, 1477–1479.
- Johnson J. E., Webb S. M., Ma C. and Fischer W. W. (2016) Manganese mineralogy and diagenesis in the sedimentary rock record. *Geochim. Cosmochim. Acta* **173**, 210–231.
- Johnson J. E., Webb S. M., Thomas K., Ono S., Kirschvink J. L. and Fischer W. W. (2013) Manganese-oxidizing photosynthesis before the rise of cyanobacteria. *Proc. Natl. Acad. Sci.* **110**, 11238–11243.
- Jones D. S. and Fike D. A. (2013) Dynamic sulfur and carbon cycling through the end-Ordovician extinction revealed by paired sulfate–pyrite $\delta^{34}\text{S}$. *Earth Planet. Sci. Lett.* **363**, 144–155.
- Jørgensen B. B., Isaksen M. F. and Jannasch H. W. (1992) Bacterial sulfate reduction above 100 °C in deep-sea hydrothermal vent sediments. *Science* **258**, 1756–1757.
- Jørgensen B. B. and Kasten S. (2006) Sulfur cycling and methane oxidation. In *Marine Geochemistry* (eds. H. D. Schulz and M. Zabel). Springer-Verlag, pp. 271–309.
- Kaplan I. R. and Rafter T. A. (1958) Fractionation of stable isotopes of sulfur by Thiobacilli. *Science* **127**, 517–518.
- Kaplan I. R. and Rittenberg S. C. (1964) Microbiological fractionation of sulphur isotopes. *Microbiology* **34**, 195–212.
- Kampschulte A. and Strauss H. (2004) The sulfur isotopic evolution of Phanerozoic seawater based on the analysis of structurally substituted sulfate in carbonates. *Chem. Geol.* **204**, 255–286.
- King H. E., Walters C. C., Horn W. C., Zimmer M., Heines M. M., Lamberti W. A., Kliewer C., Pottorf R. J. and Macleod G.

- (2014) Sulfur isotope analysis of bitumen and pyrite associated with thermal sulfate reduction in reservoir carbonates at the Big Piney-La Barge production complex. *Geochem. Cosmochim. Acta* **134**, 210–220.
- Kiyosu Y. and Krouse H. R. (1990) The role of organic acid in the abiogenic reduction of sulfate and the sulfur isotope effect. *Geochem. J.* **24**, 21–27.
- Kiyosu Y. (1980) Chemical reduction and sulfur-isotope effects of sulfate by organic matter under hydrothermal conditions. *Chem. Geol.* **30**, 47–56.
- Kohn M. J., Riciputi L. R., Stakes D. and Orange D. L. (1998) Sulfur isotope variability in biogenic pyrite: Reflections of heterogeneous bacterial colonization? *Am. Mineral.* **83**, 1454–1468.
- Konhauser K. O., Amskold L., Lalonde S. V., Posth N. R., Kappler A. and Anbar A. (2007) Decoupling photochemical Fe (II) oxidation from shallow-water BIF deposition. *Earth Planet. Sci. Lett.* **258**, 87–100.
- Konhauser K. O., Planavsky N. J., Hardisty D. S., Robbins L. J., Warchola T. J., Haugaard R., Lalonde S. V., Partin C. A., Oonk P. B. H., Tsikos H., Lyons T. W., Bekker A. and Johnson C. M. (2017) Iron formations: a global record of Neoproterozoic to Palaeo-proterozoic environmental history. *Earth-Sci. Rev.* **172**, 140–177.
- Leavitt W. D., Bradley A. S., Halevy I. and Johnston D. T. (2013) Influence of sulfate reduction rates on the Phanerozoic sulfur isotope record. *Proc. Natl. Acad. Sci.* **110**, 11244–11249.
- Li C., Love G. D., Lyons T. W., Scott C. T., Feng L. J., Huang J., Chang H. J., Zhang Q. and Chu X. L. (2012) Evidence for a redox stratified Cryogenian marine basin, Datangpo Formation, South China. *Earth Planet. Sci. Lett.* **331–332**, 246–256.
- Li L., Wing B. A., Bui T. H., McDermott J. M., Slater G. F., Wei S., Lacrampe-Couloume G. and Sherwood Lollar B. (2016) Sulfur mass-independent fractionation in subsurface fracture waters indicates a long-standing sulfur cycle in Precambrian rocks. *Nat. Commun.* **7**, 13252.
- Li Y. (2007) *Metallogenic Regularity and Prospecting Direction of Hotwater Sedimentary Deposits, Guangxi, China (Ph.D. thesis)*. Central South University, p. 229 (in Chinese with English abstract).
- Liu T. B., Maynard J. B. and Alten J. (2006) Superheavy S isotopes from glacier-associated sediments of the Neoproterozoic of south China: Oceanic anoxia or sulfate limitation? *Geol. Soc. Am. Memoirs* **198**, 205–222.
- Lowenstein T. K., Hardie L. A., Timofeeff M. N. and Demicco R. V. (2003) Secular variation in seawater chemistry and the origin of calcium chloride basinal brines. *Geology* **31**, 857–860.
- Ma X. P., Gong Y. M., Chen D. Z., Racki G., Chen X. Q. and Liao W. H. (2016) The Late Devonian Frasnian-Famennian Event in South China — Patterns and causes of extinctions, sea level changes, and isotope variations. *Palaeogeogr. Palaeoclimatol. Palaeoecol.* **448**, 224–244.
- Ma Y. S., Chen H. D., Wang G. L., Guo T. L., Tian J. C., Liu W. J., Xu X. S., Zheng R. C., Mou C. L. and Hou M. C. (2009) *Sequence stratigraphy and Paleogeography in south China*. China Science Publishing, Beijing, pp. 289–291 (in Chinese with English abstract).
- Machel H. G. (2001) Bacterial and thermochemical sulfate reduction in diagenetic settings old and new insights. *Sediment. Geol.* **140**, 143–175.
- Machel H. G., Krouse H. R. and Sassen R. (1995) Products and distinguishing criteria of bacterial and thermochemical sulfate reduction. *App. Geochem.* **10**(4), 373–389.
- Marin-Carbonne J., Remusat L., Sforza M. C., Thomazo C., Cartigny P. and Philippot P. (2018) Sulfur isotope's signal of nanopyrates enclosed in 2.7 Ga stromatolitic organic remains reveal microbial sulfate reduction. *Geobiology* **16**, 121–138.
- Marini L., Moretti R. and Accornero M. (2011) Sulfur isotopes in magmatic-hydrothermal systems, melts, and magmas. *Rev. Mineral. Geochem.* **73**, 423–492.
- Maynard J. B. (2010) The chemistry of manganese ores through time: a signal of increasing diversity of earth-surface environments. *Econ. Geol.* **105**(3), 535–552.
- McLoughlin N., Grosch E. G., Kilburn M. R. and Wacey D. (2012) Sulfur isotope evidence for a Paleoproterozoic subseafloor biosphere, Barberton, South Africa. *Geology* **40**, 1031–1034.
- Meshoulam A., Ellis G. S., Ahmad W. S., Deev A., Sessions A. L., Tang Y. C., Adkins J. F., Liu J. Z., Gilhooly, III, W. P., Aizenshtat Z. and Amrani A. (2016) Study of thermochemical sulfate reduction mechanism using compound specific sulfur isotope analysis. *Geochim. Cosmochim. Acta* **188**, 73–92.
- Metcalf I. (2006) Palaeozoic and Mesozoic tectonic evolution and palaeogeography of East Asian crustal fragments: The Korean Peninsula in context. *Gondwana Res.* **9**, 24–46.
- Newton R. J., Reeves E. P., Kafousia N., Wignall P. B., Bottrell S. H. and Sha J. G. (2011) Low marine sulfate concentrations and the isolation of the European epicontinental sea during the Early Jurassic. *Geology* **39**, 7–10.
- Oduro H., Harms B., Sintim H. O., Kaufman A. J., Cody G. and Farquhar J. (2011) Evidence of magnetic isotope effects during thermochemical sulfate reduction. *Proc. Natl. Acad. Sci.* **108**, 17635–17638.
- Ohmoto H. (1972) Systematics of sulfur and carbon isotopes in hydrothermal ore deposits. *Econ. Geol.* **67**, 551–578.
- Ohmoto H. (1992) Biogeochemistry of sulfur and the mechanisms of sulfide-sulfate mineralization in Archean oceans. In *Early Organic Evolution, Implications for Mineral and Energy Resources* (eds. M. Schidlowski, S. Golubic, M. M. Kimberley, D. M. McKirdy and P. A. Trudinger). Springer-Verlag, pp. 378–397.
- Ohmoto H. and Goldhaber M. B. (1997) Sulfur and carbon isotopes. In *Geochemistry of Hydrothermal Ore Deposits* (ed. H. L. Barnes), third ed. Wiley, pp. 517–611.
- Ohmoto H. and Lasaga A. C. (1982) Kinetics of reactions between aqueous sulfates and sulfides in hydrothermal systems. *Geochim. Cosmochim. Acta* **46**, 1727–1745.
- Ohmoto H. and Rye R. O. (1979) Isotopes of sulfur and carbon. In *Geochemistry of Hydrothermal Ore Deposits* (ed. H. L. Barnes). Wiley, New York, pp. 509–567.
- Okita P. M. and Shanks W. C. (1992) Origin of stratiform sediment-hosted manganese carbonate ore deposits: Examples from Molango Mexico, and Taojiang, China. *Chem. Geol.* **99**, 139–164.
- Pasquier V., Sansjofre P., Rabineau M., Revillon S., Houghton J. and Fike D. A. (2017) Pyrite sulfur isotopes reveal glacial interglacial environmental changes. *Proc. Natl. Acad. Sci.* **114** (23), 5941–5945.
- Paytan A. and Gray E. T. (2012) Sulfur Isotope stratigraphy. In *The Geologic Timescale 212* (eds. F. M. Gradstein, J. G. Ogg, M. Schmitz and G. Ogg). Elsevier, Amsterdam, pp. 167–180.
- Polgári M., Németh T., Pál-Molnár E., Futó I., Vigh T. and Mojzsis S. J. (2016) Correlated chemostratigraphy of Mn-carbonate microbialites (Úrkút, Hungary). *Gondwana Res.* **29**, 278–289.
- Powell T. G. and Macqueen R. W. (1984) Precipitation of sulfide ores and organic matter – sulfate reactions at pine point, Canada. *Science* **224**(4644), 63–66.
- Qin Y. K., Zhang H. C. and Yao J. Q. (2010) Geochemical characteristics and geological implication of the Xialei Manganese Deposit, Daxin County, Guangxi. *Geol. Rev.* **56**, 664–672 (in Chinese with English abstract).

- Qiu W. H. J., Zhou M. F., Li X., Williams-Jones A. E. and Yuan H. (2018) The Genesis of the Giant Dajiangping SEDEX-Type Pyrite Deposit, South China. *Econ. Geol.* **113**(6), 1419–1446.
- Richardson J. A., Keating C., Lepland A., Hints O., Bradley A. S. and Fike D. A. (2019a) Silurian records of carbon and sulfur cycling from Estonia: the importance of depositional environment on isotopic trends. *Earth Planet. Sci. Lett.* **512**, 71–82.
- Richardson J. A., Newville M., Lanzirrotti A., Webb S. M., Rose C. V., Catalano J. G. and Fike D. A. (2019b) Depositional and diagenetic constrains on the abundance and spatial variability of carbonate-associated sulfate. *Chem. Geol.* **523**, 59–72.
- Ries J. B., Fike D. A., Pratt L. M., Lyons T. W. and Grotzinger J. P. (2009) Superheavy pyrite ($\delta^{34}\text{S}_{\text{py}} > \delta^{34}\text{S}_{\text{CAS}}$) in the terminal Proterozoic Nama Group, southern Namibia; A consequence of low seawater sulfate at the dawn of animal life. *Geology* **37**, 743–746.
- Rose C. V., Fischer W. W., Finnegan S. and Fike D. A. (2019) Records of carbon and sulfur cycling during the Silurian Ireviken Event in Gotland, Sweden. *Geochim. Cosmochim. Acta* **246**, 299–316.
- Seal R. R. (2006) Sulfur isotope geochemistry of sulfide minerals. Sulfide mineralogy and geochemistry (ed. D. J. Vaughan). *Rev. Mineral. Geochem.* **61**, 633–677.
- Seccombe P. K., Spry P. G., Both R. A., Jones M. T. and Schiller J. C. (1985) Base metal mineralization in the Kanmantoo Group, South Australia: a regional sulfur isotope study. *Econ. Geol.* **80**, 1824–1841.
- Sakai H. and Dickson F. W. (1978) Experimental determination of the rate and equilibrium fractionation factors of sulfur Isotope exchange between sulfate and sulfide in slightly acid solutions at 300 °C and 1000 bars. *Earth Planet. Sci. Lett.* **39**, 151–161.
- Shanks, III, W. C., Bischoff J. L. and Rosenbauer R. J. (1981) Seawater sulfate reduction and sulfur isotope fractionation in basaltic systems: Interaction of seawater with fayalite and magnetite at 200–350°C. *Geochim. Cosmochim. Acta* **45**, 1977–1995.
- Shanks, III, W. C., Böhlke J. K. and Seal R. R. (1995) Stable isotopes in midocean ridge hydrothermal systems: interaction between fluids, minerals and organisms. In *Seafloor Hydrothermal Systems: Physical, Chemical, Biological, and Geological Interactions. GeophysMon 91* (eds. S. E. Humphris, R. A. Zierenberg, L. S. Mullineaux and R. E. Thomson). American Geophysical Union, Washington, DC, pp. 194–221.
- Sim M. S., Bosak T. and Ono S. (2011a) Large sulfur isotope fractionation does not require disproportionation. *Science* **333**, 74–77.
- Sim M. S., Ono S., Donovan K., Templer S. P. and Bosak T. (2011b) Effect of electron donors on the fractionation of sulfur isotopes by a marine Desulfobivrio sp. *Geochim. Cosmochim. Acta* **75**, 4244–4259.
- Sim M. S., Ono S. and Hurtgen M. T. (2015) Sulfur isotope evidence for low and fluctuating sulfate levels in the Late Devonian Ocean and the potential link with the mass extinction event. *Earth Planet. Sci. Lett.* **419**, 52–62.
- Song J. J., Crasquin S. and Gong Y. M. (2018) Ostracods (Crustacea) as shelf to basin indicators: evidence from Late Devonian Yangdi and Nandong sections in Guangxi, South China. *J. Micropaleontol.* **37**, 257–281.
- Ulrich T., Long D. G. F., Kamber B. S. and Whitehouse M. J. (2011) In situ trace element and sulfur isotope analysis of pyrite in a Paleoproterozoic Gold Placer Deposit, Pardo and Clement Townships, Ontario, Canada. *Econ. Geol.* **106**, 667–686.
- Wacey D., Kilburn M. R., Saunders M., Cliff J. B., Kong C., Liu A. G., Matthews J. J. and Brasier M. D. (2015) Uncovering framboidal pyrite biogenicity using nano-scale CNorg mapping. *Geology* **43**, 27–30.
- Wagner T. and Boyce A. J. (2006) Pyrite metamorphism in the Devonian Hunsrück slate of Germany: insights from laser microprobe sulfur isotope analysis and thermodynamic modeling. *Am. J. Sci.* **306**, 525–552.
- Wagner T., Boyce A. J., Jonsson E. and Fallick A. E. (2004) Laser microprobe sulphur isotope analysis of arsenopyrite: experimental calibration and application to the Boliden Au–Cu–As massive sulphide deposit. *Ore Geol. Rev.* **25**, 311–325.
- Wang K., Geldsetzer H., Goodfellow W. D. and Krouse H. R. (1996) Carbon and sulfur isotope anomalies across the Frasnian–Famennian extinction boundary, Alberta, Canada. *Geology* **24**, 187–191.
- Williford K. H., Van Kranendonk M. J., Ushikubo T., Kozdon R. and Valley J. W. (2011) Constraining atmospheric oxygen and seawater sulfate concentrations during Paleoproterozoic glaciation: In situ sulfur three-isotope microanalysis of pyrite from the Turee Creek Group, Western Australia. *Geochim. Cosmochim. Acta* **75**, 5686–5705.
- Wing B. A. and Halevy I. (2014) Intracellular metabolite levels shape sulfur isotope fractionation during microbial sulfate respiration. *Proc. Natl. Acad. Sci.* **111**, 18116–18125.
- Worden R. H., Smalley P. C. and Oxtoby N. H. (1995) Gas souring by thermochemical sulfate reduction at 140 °C. *AAPG Bull.* **79**, 854–863.
- Yang J. H., Cawood P. A., Du Y. S., Huang H. and Hu L. S. (2012) Detrital record of indosinian mountain building in sw china: provenance of the middle triassic turbidites in the youjiang basin. *Tectonophysics* **574**, 105–117.
- Zeng Y. F., Zhang J. Q., Liu W. J., Zhou H. L., Chen H. D., Xu X. H., Mao X. D. and Yang D. L. (1993) *Devonian Lithofacies Paleogeography and Mineralization in South China*. Geological Publishing House, Beijing, pp. 43–45 (in Chinese with English abstract).
- Zeng Y. Y. and Liu T. B. (1999) Characteristics of the Devonian Xialei manganese deposit, Guangxi Zhuang Autonomous Region, China. *Ore Geol. Rev.* **15**, 153–163.
- Zhang R. X. and Yang S. Y. (2016) A mathematical model for determining carbon coating thickness and its application in electron probe microanalysis. *Microsc. Microanal.* **22**(6), 1374–1380.
- Zhu Z. Y., Cook N. J., Yang T., Ciobanu C. L., Zhao K. D. and Jiang S. Y. (2016) Mapping of sulfur isotopes and trace elements in sulfides by LA-(MC)-ICP-MS: potential analytical problems, improvements and implications. *Miner.* **6**, 110.